The Astrophysical Journal, 796:129 (18pp), 2014 December 1 doi:10.1088/0004-637X/796/2/129

A PULSATION SEARCH AMONG YOUNG BROWN DWARFS AND VERY-LOW-MASS STARS

Ann Marie Cody[1,2] and Lynne A. Hillenbrand[1]
[1] California Institute of Technology, Department of Astrophysics, MC 249-17, Pasadena, CA 91125, USA; amc@ipac.caltech.edu
[2] Spitzer Science Center, California Institute of Technology, 1200 East California Boulevard, Pasadena, CA 91125, USA
Received 2014 September 10; accepted 2014 October 17; published 2014 November 14

ABSTRACT

In 2005, Palla & Baraffe proposed that brown dwarfs (BDs) and very-low-mass stars (VLMSs; < 0.1 solar masses) may be unstable to radial oscillations during the pre-main-sequence deuterium burning phase. With associated periods of one to four hours, this potentially new class of pulsation offers unprecedented opportunities to probe the interiors and evolution of low-mass objects in the 1–15 million year age range. Following up on reports of short-period variability in young clusters, we designed a high-cadence photometric monitoring campaign to search for deuterium-burning pulsation among a sample of 348 BDs and VLMSs in the four young clusters σ Orionis, Chamaeleon I, IC 348, and Upper Scorpius. In the resulting light curves we achieved sensitivity to periodic signals of amplitude several millimagnitudes, on timescales from 15 minutes to two weeks. Despite the exquisite data quality, we failed to detect any periodicities below seven hours. We conclude that D-burning pulsations are not able to grow to observable amplitudes in the early pre-main sequence. In spite of the nondetection, we did uncover a rich set of variability behavior—both periodic and aperiodic—on day to week timescales. We present new compilations of variable sources from our sample, as well as three new candidate cluster members in Chamaeleon I.

Key words: brown dwarfs – open clusters and associations: individual (Chamaeleon I, IC 348, σ Orionis, Upper Scorpius) – stars: low-mass – stars: oscillations – stars: variables: general

Online-only material: color figures

1. PULSATION IN YOUNG STARS AND BROWN DWARFS

Investigation of the interiors and evolutionary states of stars has long been a challenging task. Measurements of mass and age rely heavily on theoretical models, many of which require further calibration. This situation has begun to improve dramatically with the rise of asteroseismology. Precision measurements of stellar oscillation frequencies and their differences can furnish ages and masses to better than 10% (e.g., Lebreton & Goupil 2014), and even internal rotation profiles (e.g., Kurtz et al. 2014; Beck et al. 2012).

One of the obvious limitations of asteroseismology is that it applies only to stars that are unstable to pulsation. Traditionally this has omitted most young and low-mass stars. Recently, the first pre-main sequence (PMS) pulsating stars at intermediate masses have been identified and characterized in young open clusters (Zwintz 2008; Guenther et al. 2009). These PMS δ Scuti stars inhabit an instability strip in the Hertzsprung–Russell (H-R) diagram comprising spectral types A to F ($M \sim 1.5$–$3\ M_{\odot}$). Observations of their pulsations have now been used to demonstrate a relationship between oscillation frequencies and evolutionary status (Zwintz et al. 2014).

For stars less than $1.5\ M_{\odot}$, asteroseismology has yet to yield fruit. Brown dwarfs (BDs) and very-low-mass stars (VLMSs) have been predicted to undergo a pulsation instability fueled by central deuterium burning (e.g., Palla & Baraffe 2005, hereafter PB05). The pulsation theory involves destabilization via the epsilon mechanism—a conversion of nuclear energy to kinetic oscillations. In brief, their main predictions are that deuterium burning BDs and VLMSs from $\sim$0.02 to $0.1\ M_{\odot}$ will exhibit radial oscillations with periods from one to four hours. The amplitudes are indeterminate, but the PB05 calculations indicate that pulsations will grow exponentially with time if they are not damped in the stellar interior by, e.g., convection. They argue that the mismatch between the pulsation timescale and the convective overturn timescale ($\sim$weeks, apart from the surface layers where it is shorter) rules out the damping scenario. Empirical verification of this instability theory through detection of short-timescale periodic variability presents a new opportunity to probe the interior and surface properties of young low-mass objects. In support of the pulsation hypothesis are several previous claims of short-period variability with reported flux changes at the few to five percent level (e.g., Scholz & Eislöffel 2004; Bailer-Jones & Mundt 2001; Zapatero Osorio et al. 2003).

To verify or refute these findings, we initiated a pulsation search in the σ Orionis cluster (Cody & Hillenbrand 2010, 2011), where we encountered over 100 periodic and aperiodic variables. The conclusion of that work was that none of the light curves exhibited behavior consistent with deuterium burning oscillations on few-hour timescales. We now report the result of an expanded campaign in three other young star-forming regions: IC 348, Chamaeleon I, and the Upper Scorpius association. The expanded sample enables better coverage of parameter space in the H-R diagram, as well as improved statistical constraint on pulsation amplitudes. In addition to searching for short-period oscillations, we have also mined these fields for longer timescale variability and new cluster members.

2. TARGET SELECTION AND OBSERVATIONS

The prospect of detecting pulsation in young BDs and VLMSs is dependent on the existence of a suitable observational sample with characteristics in the range of the prospective pulsators. Because the pulsation instability strip calculated by PB05 is fairly narrow compared to the characteristic range of luminosities observed in 1–10 Myr clusters, most very low mass members of a young, roughly coeval population may not be expected to pulsate. Yet substantial uncertainties in luminosity

Table 1
Photometric Observations Comprising the Pulsation Search Campaign

Cluster	Telescope	Instrument	Field center (R.A., Decl.)	FOV	Dates	Duty cycle	Cadence (seconds)	Band
σ Ori	CTIO 1.0 m	Y4KCam	5:38:00.6, −02:43:44	$20' \times 20'$	2007 Dec 27–2008 Jan 7,	25%	460	I, R
Cha I	CTIO 1.0 m	Y4KCam	11:09:51.0, −77:27:44	$20' \times 20'$	2008 May 13–25	25%	700	i, r
USco	CTIO 1.0 m	Y4KCam	16:11:08, −22:12:04	$20' \times 20'$	2008 May 13–16; 21–22	15%	700	i, r
USco	CTIO 1.0 m	Y4KCam	16:17:57.5, −23:45:41	$20' \times 20'$	2008 May 23–25	15%	700	i, r
USco	P60	(CCD)	16:13:17.5, −19:27:00	$12\farcm5 \times 12\farcm5$	2008 Jun 1–14	13%	330	ip
IC 348	P60	(CCD)	3:44:21.8, +32:05:43	$12\farcm5 \times 12\farcm5$	2008 Nov 17–23, Nov 28–29	18%	270	ip, Cr
σ Ori	CTIO 1.0 m	Y4KCam	5:39:31.1, −02:37:26	$20' \times 20'$	2008 Dec 14–24	28%	700	I, R
USco	P60	(CCD)	16:17:46.3, −20:54:18	$12\farcm5 \times 12\farcm5$	2009 May 14–30	13%	330	ip, rp
σ Ori	*Spitzer*	IRAC	05:38:23.3, −02:40:29	$5\farcm2 \times 5\farcm2$	2009 Oct 22–23	100%	31	3.6 μm
σ Ori	*Spitzer*	IRAC	05:38:26.4, −02:47:13	$5\farcm2 \times 5\farcm2$	2009 Oct 22–23	100%	31	4.5 μm
IC 348	*HST*	WFC3	03:44:19.5, +32:06:20	$162'' \times 81''$	2011 Jan 29–Feb 4	47%, 30%[a]	400	F814W

Notes. We list the details of each observing run in the photometric pulsation search. In the last column, lower-case band letters refer to the Sloan (SDSS) system; where *R*-band (r, R or Cr) observations are listed, there were at most two per night, to assess general colors of objects (but not enough to study variability). Abbreviations are as follows: P60 is the Palomar 60 inch telescope, *HST* is the *Hubble Space Telescope*, WFC3 is the Wide-Field Imaging Camera 3, IRAC is the *Spitzer* Infrared Array Camera. Duty cycle refers to the percentage of each day spent taking exposures (or reading out). *Note:* [a]The two duty cycles listed for the *HST* run refer to that of a single orbit (images were acquired for 46 of 97 minutes), and that of a single day (visits took place over ∼7 hr, and further observations did not resume until approximately one day later).

estimates and theoretical assumptions preclude determination of exactly which objects should display the phenomenon. To harvest enough candidate pulsators for statistical evaluation, our survey therefore relied on a large sample size. Selection of suitable clusters for the campaign involved two requirements: (1) that the known young member population extend into the substellar regime where pulsation is predicted to occur, and (2) that the members be bright enough for high-precision photometry with telescope apertures of up to a few meters. This limited the cluster distance to 500 pc. The level of extinction in some star-forming regions further restricted the number of available targets.

To assemble a list of pulsation candidates according to the above criteria, we relied on the substantial populations of VLMS and BD deuterium burning objects that have been identified in open clusters and star forming regions. Most cluster surveys to date have selected candidates based on photometric colors and confirmed membership by identifying features of youth (e.g., strong Hα emission or low-gravity lines) in follow-up spectra. However, the rich variety of phenomena in these regions, as traced by X-ray activity, photometric variability, accretion, and circumstellar disk signatures, provides alternative methods for uncovering young stellar and substellar objects. We compiled a list of the young clusters and associations with VLMSs and BDs; the regions chosen for study were σ Orionis, Chamaeleon I, Upper Scorpius, and IC 348. Ultimately, our multi-telescope monitoring program covered a significant fraction of the spectroscopically confirmed very-low-mass objects in these young star-forming areas. The 1–10 Myr range in median ages of these clusters enables testing the effect of not only mass, but also age, on our results.

To choose specific BDs and VLMSs suitable for the photometric monitoring campaign, we focused on targets with a high probability of exhibiting pulsation, based on position relative to PB05's pulsation instability strip on the H-R diagram. For most of the clusters, it was crucial to optimize the field positions to include as many pulsation candidates as possible. This task was initiated by searching the literature relevant to each of the four chosen clusters for spectral types later than M4 (corresponding to $\lesssim$0.2 $M_\odot$, and a high likelihood that they are still burning deuterium) as well as established membership, to rule out status as field dwarfs. The collected spectral types and brightnesses were then used to produce H-R diagrams and compare the positions of known BDs and VLMSs with the deuterium-burning instability strip. We detail the selected targets and the suite of observations conducted for each region below; a summary is provided in Table 1.

2.1. σ Orionis

The σ Orionis cluster was our primary target in the search for pulsation, with observations of candidate very-low-mass members in three fields. At approximately 3 Myr of age (Sherry et al. 2008), it should contain numerous stars and BDs that are still burning deuterium. Two $20' \times 20'$ fields were initially selected for monitoring with the Cerro Tololo Inter-American Observatory 1.0 m telescope ("CTIO 1.0 m") from 2007 December 27 to 2008 January 7 and from 2008 December 14 to 24. We identified VLMSs and BDs in the cluster by mining the works of Béjar et al. (1999, 2001), Barrado y Navascués et al. (2001, 2003), Béjar et al. (2004), Caballero et al. (2004), Sherry et al. (2004), Scholz & Eislöffel (2004), Burningham et al. (2005), Kenyon et al. (2005), Franciosini et al. (2006), Caballero et al. (2007), Hernández et al. (2007), Caballero (2008), Luhman et al. (2008), and Lodieu et al. (2009); a total of 153 confirmed and candidate σ Orionis members fell in the two CTIO fields, including 15 spectroscopically confirmed young BDs. Further details on the selection, as well as a full list of objects and an image of the field of view, are provided in Cody & Hillenbrand (2010, hereafter CH10).

We re-observed a subset of the CTIO targets in the infrared with the *Spitzer Space Telescope* Warm Mission in 2009, focusing on a set of five confirmed and two candidate BD members of σ Orionis. Also included in the *Spitzer* 3.6 and 4.5 μm fields were seven additional higher mass ($>0.1 M_\odot$) cluster members. All targets were monitored continuously for a single 24 hr period, at a cadence of ∼30 s. An extensive description of these observations is available in Cody & Hillenbrand (2011).

2.2. Chamaeleon I

Initial target compilation for the Chamaeleon I cluster was based on Luhman's (2007) work, plus additional members from

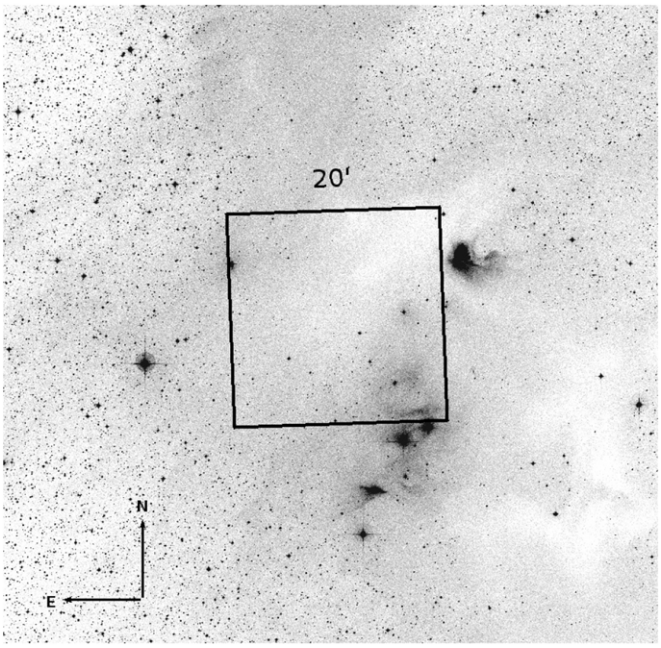

Figure 1. Cha I field observed with the CTIO 1.0 m telescope is shown superimposed on a Digital Sky Survey image. Extinction in this region is highly variable, and we have avoided the most nebulous dark cloud region toward the west.

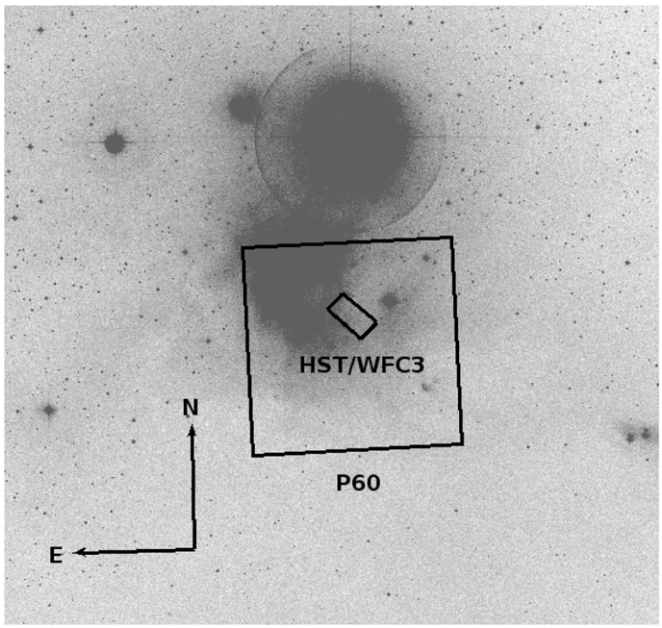

Figure 2. IC 348 fields observed with the Palomar 60 inch telescope (12.′5 × 12.′5) and *HST* (81″ × 162″) are shown superimposed on a Digital Sky Survey image. The bright B star binary o Per lies just to the north.

Luhman & Muench (2008), Luhman et al. (2008), and Mužić et al. (2011). These studies indicate a median age for the cluster of ∼2 myr, making it slightly younger than σ Orionis, and a prime candidate for the deuterium burning pulsation search. The campaign on Cha I involved observations of a single 20′ × 20′ field with the CTIO 1.0 m from 2008 May 13–25. The field of view (FOV) was selected to maximize the number of BDs monitored and also avoid some of the dense nebulosity in this region; it is displayed in Figure 1.

From the full source compilation we selected a total of 32 Cha I members for observation, of which 6 have spectral types consistent with substellar status (spectral type M6 and later) and 22 more are likely VLMSs with (M4 or later). The remaining four are higher mass stars and not expected to pulsate. We have compiled the existing photometric and spectroscopic data on the set of 32 objects, including optical through near-infrared photometry and spectral types, in Table 2.

2.3. IC 348

IC 348 is an appealing target in the search for pulsation, since it is relatively compact (<1° square), and its membership is very well characterized (Luhman et al. 2003; Muench et al. 2007). At a 2–3 myr (Luhman et al. 2003), it is comparable in age to σ Orionis and Cha I. Several previous studies have identified numerous periodic variables, which are presumably the result of rotational modulation of spots (Cohen et al. 2004; Littlefair et al. 2005; Cieza & Baliber 2006, and references therein). The typical periods are near two to three days, but several objects have reported periods as short as five hours.

We observed IC 348 from the ground with the Palomar 60 inch telescope ("P60"; Cenko et al. 2006) and from space using the *Hubble Space Telescope* (*HST*) Wide Field Camera 3 (WFC3). The ∼12.′5 × 12.′5 ground-based field of view encompassed a significant spatial extent within IC 348, including the nebulous region in the cluster center. The WFC3 field is much smaller, with a full field of view of 162″ × 162″. To maximize the data cadence for *HST* we opted to observe in the subarray mode, for which only one of two 81″ × 162″ chips was used. Since the ground-based photometry preceded the space observations by more than three years, we were able to select several faint BD pulsation candidates that required photometry at the higher sensitivity levels afforded by *HST*. Therefore the WFC3 field did not cover an additional region, but rather fell within the previous ground-based FOV, encompassing four BDs and and two VLMSs. Two of these (L761 and L1434) do not have ground-based light curves since they suffered from low signal-to-noise. Both the ground- and space-based fields are illustrated in Figure 2.

Selection of low-mass IC 348 cluster objects was carried out by considering the spectral types presented by (Luhman et al. 2003, 2005). A total of 194 members fell within the chosen ground-based FOV. However, we did not extract photometry for stars that fell on bad pixel columns, or for some BDs that were too faint for adequate signal to noise. There are also a number of brighter stars within the field for which we did not obtain data since their point-spread functions (PSFs) were saturated and distorted by nebulosity and scattered light within the central region of the cluster where several bright B stars lie. For the pulsation campaign, we ultimately monitored 147 low-mass IC 348 members, including 26 BDs (spectral types M6 or later) and 65 VLMSs (M4–M6). We present a compilation of basic target properties in Tables 3 and 4.

2.4. Upper Scorpius

The Upper Scorpius (USco) region is one of the most spatially extended young associations, with stars and BDs spread over many tens of degrees on the sky. As a result, few variability studies have been performed here, apart from the work of Slesnick (2008). It is significantly older than the other three regions studied, with age estimates from 5 to 11 myr (Preibisch et al. 2002; Pecaut et al. 2012). Nevertheless, an examination of the H-R diagram of catalogued low-mass members shows that

Table 2
Cha I Objects Observed

Object	Other ID	SpT	i	J	H	K_s
2MASS J11105076−7718031	ESO Halpha 568	M4.25	14.38	12.044 ± 0.023	11.101 ± 0.023	10.748 ± 0.024
2MASS J11105359−7725004	ISO 256	M4.5	17.51	14.271 ± 0.030	12.507 ± 0.027	11.339 ± 0.021
2MASS J11065906−7718535	ISO 89	M4.25	12.97	11.204 ± 0.026	10.423 ± 0.021	10.003 ± 0.024
2MASS J11070925−7718471	ISO 91	M3	...	14.902 ± 0.042	12.581 ± 0.021	11.476 ± 0.023
2MASS J11071668−7735532	Cha Halpha 1	M7.75	16.38	13.342 ± 0.024	12.668 ± 0.026	12.174 ± 0.024
2MASS J11071860−7732516	Cha Halpha 9	M5.5	...	13.733 ± 0.026	12.492 ± 0.023	11.803 ± 0.024
2MASS J11072040−7729403	ISO 99	M4.5	13.00	11.134 ± 0.024	10.547 ± 0.023	10.259 ± 0.021
2MASS J11073519−7734493	CHXR 76	M4.25	14.39	12.127 ± 0.023	11.279 ± 0.023	10.954 ± 0.021
2MASS J11073686−7733335	CHXR 26	M3.5	15.18	11.593 ± 0.030	10.045 ± 0.035	9.348 ± 0.027
2MASS J11073775−7735308	Cha Halpha 7	M7.75	17.03	13.613 ± 0.030	12.900 ± 0.026	12.421 ± 0.030
2MASS J11074245−7733593	Cha Halpha 2	M5.25	15.26	12.210 ± 0.024	11.243 ± 0.026	10.675 ± 0.021
2MASS J11075225−7736569	Cha Halpha 3	M5.5	15.07	12.292 ± 0.024	11.520 ± 0.023	11.097 ± 0.019
2MASS J11081850−7730408	ISO 138	M6.5	16.77	14.057 ± 0.030	13.466 ± 0.035	13.040 ± 0.032
Cha J11081938−7731522	...	M4.75	...	...	...	...
2MASS J11082238−7730277	ISO 143	M5	15.51	12.570 ± 0.024	11.651 ± 0.027	11.095 ± 0.023
2MASS J11083952−7734166	Cha Halpha 6	M5.75	15.06	12.263 ± 0.027	11.479 ± 0.024	11.038 ± 0.027
2MASS J11085421−7732115	CHXR 78C	M5.25	15.01	12.310 ± 0.026	11.555 ± 0.023	11.224 ± 0.024
2MASS J11085596−7727132	ISO 167	M5.25	17.08	13.514 ± 0.031	12.293 ± 0.026	11.619 ± 0.025
2MASS J11093543−7731390	...	M8.25	...	15.936 ± 0.092	15.022 ± 0.087	14.412 ± 0.101
2MASS J11094260−7725578	ISO 200	M5	15.91	12.329 ± 0.027	11.175 ± 0.026	10.552 ± 0.028
2MASS J11094742−7726290	ESO Halpha 567	M3.25	16.62	12.767 ± 0.027	11.228 ± 0.023	10.236 ± 0.022
2MASS J11094918−7731197	KG 102	M5.5	15.64	13.057 ± 0.036	12.229 ± 0.039	11.802 ± 0.034
2MASS J11095336−7728365	ISO 220	M5.75	...	14.300 ± 0.039	13.020 ± 0.026	12.233 ± 0.025
2MASS J11100192−7725451	LM04_419	M5.25	17.46	13.833 ± 0.032	12.605 ± 0.026	12.021 ± 0.03
2MASS J11100785−7727480	ISO 235	M5.5	17.79	13.545 ± 0.030	12.097 ± 0.026	11.342 ± 0.023
2MASS J11101153−7733521	...	M4.5	14.24	12.183 ± 0.031	11.192 ± 0.023	10.783 ± 0.019
2MASS J11103481−7722053	LM04_405	M4	...	12.038 ± 0.023	10.718 ± 0.024	10.034 ± 0.019
2MASS J11103644−7722131	ISO 250	M4.75	16.52	12.724 ± 0.027	11.369 ± 0.026	10.667 ± 0.021
2MASS J11103801−7732399	CHXR 47	K3	11.90	9.741 ± 0.027	8.687 ± 0.047	8.277 ± 0.029
2MASS J11104141−7720480	ISO 252	M6	17.29	13.860 ± 0.030	12.891 ± 0.027	12.266 ± 0.023
2MASS J11120288−7722483	...	M6	...	13.588 ± 0.030	12.941 ± 0.044	12.510 ± 0.030
2MASS J11120351−7726009	ISO 282	M4.75	...	13.626 ± 0.024	12.587 ± 0.025	11.842 ± 0.023

Notes. Spectral types and i-band magnitudes are from Luhman (2004) and Luhman (2007); J, H, and K magnitudes are from 2MASS. Objects with the alternate identification LM04 are from the catalog of Martí et al. (2004).

many objects have temperatures and luminosities overlapping the D-burning instability strip.

Because of the sparseness of this association, it is difficult to obtain data on more than one target at a time. We therefore selected fields carefully to maximize the number of pulsation candidates. We ultimately observed five different fields in Upper Scorpius, including 5 BDs and 11 VLMSs, with identifications and references listed in Table 5. None of these regions contained any nebulosity. Observations of three of the fields were abbreviated to three nights or less because of weather (the CTIO 1.0 m run), and tracking problems (USco members in the first field chosen for observation with the P60 fell too close to the edge of the detector and tended to wander out of the FOV). The list of dates is provided in Table 1. Since our observations in 2008 and 2009, further low-mass Upper Scorpius members have been discovered by Lodieu et al. (2011) and Dawson et al. (2011). We identified three of these objects from Lodieu et al. (2011) in our first FOV from CTIO 1.0 m Y4KCam monitoring in 2008 May, with no additional targets in any of the other observations.

3. DATA ACQUISITION AND REDUCTION

We employed four different telescopes in the search for pulsation, as summarized in Table 1. An extensive discussion of observations with the *Spitzer Space Telescope* is provided in Cody & Hillenbrand (2011); here we detail the observing setups with the other three facilities.

3.1. Cerro Tololo Inter-American Observatory 1.0 m Telescope

We observed low-mass targets in σ Orionis, Chamaeleon I, and Upper Scorpius with the CTIO 1.0 m. The observational setup and data reduction procedures were the nearly same for all CTIO 1.0 m runs, and they are described in detail in CH10. The selected exposure time was 600 s for all runs, apart from the first set of observations on σ Orionis members (360 s).

The main distinction for the 2008 May observing run (see Table 1) was that sky conditions were not photometric, and just over two nights were lost to clouds. In addition, telescope building maintenance caused a new accumulation of dust specks on the detector each night, which resulted in inconsistent sky flatfield acquisition. We acquired dome flatfields at the beginning and end of each night to calibrate out dust "donuts," but these dome flats are known to misrepresent the true pixel sensitivity distribution by up to 10%. Therefore, we carried out flatfielding with sky flats on nights where at least seven were available, and when clouds precluded the acquisition of sky flats, we instead relied on the dome flats but performed an illumination correction using the high signal-to-noise composite provided by P. Massey.[3]

[3] http://www.lowell.edu/users/massey/obins/y4kcamred.html

Table 3
IC 348 Cluster Members Observed with the Palomar 60 inch Telescope

Object	2MASS ID	*I*	*J*	*H*	SpT
L13	2MASS J03435964+3201539	19.46	13.45	10.78	M0.5
L23	2MASS J03443871+3208420	13.97	11.19	9.97	K3
L26	2MASS J03435602+3202132	15.62	12.29	10.56	K7
L31	2MASS J03441816+3204570	15.37	12.09	10.54	G1
L32	2MASS J03443788+3208041	14.18	11.69	10.48	K7
L35	2MASS J03443924+3207355	13.21	10.83	9.95	K3
L37	2MASS J03443798+3203296	13.18	11.45	10.44	K6
L40	2MASS J03442972+3210398	14.10	11.93	10.76	K8
L41	2MASS J03442161+3210376	14.99	12.49	11.28	K7
L46	2MASS J03441162+3203131	16.24	12.78	11.22	G8
L48	2MASS J03443487+3206337	13.45	11.50	10.60	K5.5
L49	2MASS J03435759+3201373	19.63	14.56	11.89	M0.5
L51	2MASS J03441297+3201354	19.56	15.09	12.43	...
L52	2MASS J03444351+3207427	14.98	12.12	10.89	M1
L55	2MASS J03443137+3200140	18.06	13.63	11.65	M0.5
L56	2MASS J03440499+3209537	13.02	11.55	10.71	K3.5
L58	2MASS J03443854+3208006	14.24	11.94	10.90	M1.25
L61	2MASS J03442228+3205427	15.23	12.54	11.27	K8
L65	2MASS J03443398+3208541	13.69	11.85	10.98	M0
L66	2MASS J03442847+3207224	13.53	11.67	10.85	K6.5
L68	2MASS J03442851+3159539	14.16	12.00	11.13	M3.5
L69	2MASS J03442702+3204436	13.69	11.95	11.14	M1
L71	2MASS J03443257+3208558	14.32	12.11	11.13	M3
L72	2MASS J03442257+3201536	14.31	12.12	11.15	M2.5
L74	2MASS J03443426+3210497	14.36	12.14	11.13	M2
L75	2MASS J03444376+3210304	14.26	12.75	11.60	M1.25
L82	2MASS J03443740+3206118	13.89	12.09	11.15	K7
L83	2MASS J03443741+3209009	14.93	12.49	11.44	M1
L91	2MASS J03443919+3209448	14.76	12.59	11.52	M2
L92	2MASS J03442366+3206465	14.20	12.24	11.37	M2.5
L97	2MASS J03442554+3206171	15.98	12.82	11.59	M2.25
L98	2MASS J03443860+3205064	14.88	12.47	11.52	M4
L99	...	14.78	12.89	11.90	M3.75
L103	2MASS J03444458+3208125	15.73	12.89	11.87	M2
L105	2MASS J03441125+3206121	14.32	12.39	11.47	M0
L108	2MASS J03443869+3208567	14.46	12.49	11.57	M3.25
L115	2MASS J03442999+3209210	17.18	13.58	12.02	M2.5
L116	2MASS J03442155+3210174	14.57	12.66	11.70	M1.5
L119	2MASS J03442125+3205024	15.19	12.80	11.84	M2.5
L123	2MASS J03442457+3203571	15.36	12.85	11.81	M1
L124	2MASS J03435463+3200298	14.90	12.57	11.73	M4.25
L125	2MASS J03442166+3206248	14.56	12.52	11.59	M2.75
L128	2MASS J03442017+3208565	14.84	12.73	11.83	M2
L140	2MASS J03443568+3203035	15.78	13.47	12.31	M3.25
L142	2MASS J03435619+3208362	14.65	12.63	11.73	M0
L145	2MASS J03444129+3210252	14.69	12.65	11.80	M4.75
L146	2MASS J03444261+3206194	13.99	12.55	11.74	M1
L149	2MASS J03443698+3208342	15.66	13.07	12.10	M4.75
L153	2MASS J03444276+3208337	15.95	13.21	12.22	M4.75
L156	2MASS J03440678+3207540	15.31	13.00	12.12	M4.25
L158	2MASS J03444016+3209129	16.50	13.36	12.25	M5
L159	2MASS J03444760+3210555	16.60	13.57	12.29	M4.25
L160	2MASS J03440257+3201348	14.87	12.74	12.03	M4.75
L163	2MASS J03441122+3208161	15.12	12.78	12.07	M5.25
L165	2MASS J03443545+3208563	16.15	13.28	12.33	M5.25
L166	2MASS J03444256+3210025	16.85	13.65	12.43	M4.25
L167	2MASS J03444116+3210100	16.71	14.04	12.62	M3
L168	2MASS J03443134+3210469	15.84	13.52	12.40	M4.25
L169	2MASS J03441776+3204476	15.78	13.15	12.28	M5.25
L174	2MASS J03440410+3207170	15.01	13.02	12.13	M1.5
L182	2MASS J03441820+3209593	15.74	13.21	12.30	M4.25
L187	2MASS J03440613+3207070	16.36	13.31	12.42	M4.25
L190	2MASS J03442922+3201157	17.93	14.33	12.86	M3.75
L192	2MASS J03442364+3201526	18.54	14.47	12.97	M4.5
L194	2MASS J03442724+3210373	15.88	13.74	12.66	M4.75
L198	2MASS J03443444+3206250	16.07	13.38	12.54	M5.5

Table 3
(Continued)

Object	2MASS ID	*I*	*J*	*H*	SpT
L199	2MASS J03435721+3201337	...	...	...	M6.5
L203	2MASS J03441810+3210534	18.24	16.04	13.90	M0.75
L205	2MASS J03442980+3200545	16.46	13.58	12.82	M6
L207	2MASS J03443030+3207426	17.16	14.01	12.70	M3.5
L210	2MASS J03442001+3206455	15.81	13.52	12.59	M3.5
L215	2MASS J03442894+3201378	...	...	...	M3.25
L217	2MASS J03444303+3210151	16.07	13.54	12.64	M5
L221	2MASS J03444024+3209331	16.57	14.11	13.03	M4.5
L228	...	18.28	15.07	13.43	M0.5
L230	2MASS J03443551+3208046	16.30	13.66	12.78	M5.25
L234	2MASS J03444520+3201197	...	...	...	M5.75
L237	2MASS J03442356+3209338	15.74	13.56	12.76	M5
L243	2MASS J03440770+3205050	16.71	14.01	12.98	M4.5
L252	2MASS J03442912+3207573	15.79	13.70	12.88	M4.5
L253	2MASS J03443165+3206534	16.10	13.58	12.82	M5.5
L254	2MASS J03435379+3207303	16.07	13.71	12.87	M4.25
L255	2MASS J03443569+3204527	16.10	13.70	13.01	M5.75
L256	2MASS J03435526+3207533	16.08	13.61	12.99	M5.75
L259	2MASS J03440362+3202341	16.44	13.54	12.88	M5
L266	...	16.04	13.73	12.93	M4.75
L276	2MASS J03440920+3202376	19.06	14.97	13.55	M0
L277	2MASS J03443943+3210081	16.06	13.91	13.10	M5
L278	2MASS J03443103+3205460	16.75	14.03	13.18	M5.5
L287	2MASS J03444111+3208073	17.97	14.59	13.45	M5.25
L298	2MASS J03443886+3206364	16.60	13.98	13.26	M6
L300	2MASS J03443896+3203196	16.40	14.11	13.35	M5
L301	2MASS J03442270+3201423	18.70	15.15	13.80	M4.75
L302	2MASS J03442027+3205437	17.04	14.24	13.32	M4.75
L303	2MASS J03440442+3204539	16.60	14.06	13.38	M5.75
L308	2MASS J03442122+3201144	21.03	16.18	14.24	M4
L312	2MASS J03435508+3207145	16.80	14.12	13.44	M6
L314	2MASS J03442256+3201277	18.80	15.13	13.80	M5
L322	2MASS J03441959+3202247	17.53	14.74	13.70	M4.25
L324	2MASS J03444522+3210557	17.14	14.56	13.65	M5.75
L325	2MASS J03443005+3208489	17.55	14.63	13.75	M6
L329	2MASS J03441558+3209218	17.64	14.57	13.85	M7.5
L334	2MASS J03442666+3202363	16.88	14.42	13.69	M5.75
L335	2MASS J03444423+3208473	17.34	14.56	13.76	M5.75
L336	2MASS J03443237+3203274	17.63	14.86	14.02	M5.5
L342	2MASS J03444130+3204534	17.02	14.49	13.66	M5
L350	2MASS J03441918+3205599	16.91	14.32	13.60	M5.75
L351	2MASS J03442575+3209059	17.62	14.69	13.76	M5.5
L353	2MASS J03443814+3210215	16.87	14.46	13.70	M6
L355	2MASS J03443920+3208136	18.17	14.88	14.03	M8
L358	2MASS J03441276+3210552	16.79	14.61	13.92	M5.5
L360	2MASS J03444371+3210479	16.40	14.54	13.84	M4.75
L363	2MASS J03441726+3200152	17.97	14.92	14.16	M8
L365	2MASS J03441022+3207344	17.26	14.64	13.92	M5.75
L366	2MASS J03443501+3208573	17.33	14.84	14.05	M4.75
L367	2MASS J03435915+3205567	17.36	14.68	13.95	M5.75
L373	2MASS J03442798+3205196	17.18	14.84	14.14	M5.5
L382	2MASS J03443095+3202441	18.95	15.48	14.47	M5.5
L391	2MASS J03444658+3209017	18.63	15.38	14.41	M5.75
L396	2MASS J03440233+3210154	17.57	14.98	14.18	M5.25
L405	...	18.34	15.20	14.48	M8
L414	2MASS J03444428+3210368	17.68	15.41	14.68	M5.25
L415	2MASS J03442997+3209394	18.43	15.20	14.36	M6.5
L432	2MASS J03444593+3203567	18.18	15.14	14.27	M5.75
L437	2MASS J03435638+3209591	18.61	15.41	14.62	M7.25
L454	2MASS J03444157+3210394	17.81	15.38	14.61	M5.75
L462	2MASS J03442445+3201437	19.18	15.67	14.58	M3
L468	2MASS J03441106+3201436	20.55	16.53	15.42	M8.25
L555	2MASS J03444121+3206271	16.86	14.28	13.54	M5.75
L603	2MASS J03443341+3210314	19.95	16.33	15.61	M8.5
L611	2MASS J03443035+3209446	19.61	16.35	15.49	M8
L613	2MASS J03442685+3209257	19.80	16.86	16.01	M8.25

Table 3
(Continued)

Object	2MASS ID	*I*	*J*	*H*	SpT
L622	···	20.13	17.54	16.91	M6
L690	2MASS J03443638+3203054	20.02	16.62	15.78	M8.75
L703	2MASS J03443661+3203442	20.10	16.65	15.70	M8
L705	···	20.93	17.11	16.27	M9
L725	···	20.91	18.16	17.37	M6
L738	···	20.92	17.47	16.90	M8.75
L1683	2MASS J03441583+3159367	···	···	···	M5.25
L1684	2MASS J03442330+3201544	17.29	14.78	14.05	M5.75
L1889	2MASS J03442135+3159327	···	···	···	···
L1925	2MASS J03440576+3200010	···	···	···	M5.5
L4011	···	···	···	···	···
L4044	···	21.47	17.52	16.59	M9
L30003	2MASS J03435925+3202502	···	···	···	M6

Note. Identifications beginning with "L" are from the compilation of Luhman et al. (2003) and references therein, as are the photometry and spectral types.

Table 4
IC 348 Cluster Members Observed with the *Hubble Space Telescope*

Object	*I*	*J*	*H*	SpT
L302	17.04	14.24	13.32	M4.75
L350	16.91	14.32	13.60	M5.75
L405	18.34	15.20	14.48	M8
L761	20.03	15.66	15.33	M7
L1434	21.11	18.39	17.44	M6
L4044	21.47	17.52	16.59	M9

Notes. All information is from the compilation of Luhman et al. (2003), and references therein.

3.2. Palomar 60 inch Telescope

We used the P60 robotic telescope to observe BDs and VLMSs in the IC 348 cluster, as well as additional BDs in Upper Scorpius. Observations of IC 348 took place on a total of nine nights between 2008 November 17 and November 29. The chosen field center was R.A. = $03^h44^m19\overset{s}{.}7$, decl. = $+32°04'29''$s (J2000), but since the P60 system was at that time subject to tracking inaccuracies, this position shifted up to 45″ throughout the run. We observed USco with the P60 during two different runs, from 2008 June 1 to 14, as well as 2009 May 14–30.

We chose exposure times of 240 or 300 s in the i' band to provide good sensitivity to the faint BDs without elongating the PSFs too much due to the lack of guiding. The established data reduction pipeline for the P60 performs basic calibrations, including bias subtraction, flatfielding, and fitting of the world coordinate system (Cenko et al. 2006). Although we obtained a series of sky flatfields, we determined that the domeflat images used by the pipeline were sufficient to correct interpixel sensitivity variations. Image alignment was also carried out with ease, since an accurate coordinate system was already superimposed on the calibrated images; we used the *IRAF* task *wregister* to complete this task.

3.3. HST

We used the *HST* WFC3 ultraviolet/visible (UVIS) CCD to observe pulsation candidates in IC 348. The UVIS channel is comprised of two chips, each with 4096 × 2051 pixels; since we observed in subarray mode, we used only one of these (UVIS1). Each pixel is ∼0.″04 across, for a total subarray field of view of ∼81″ × 162″.

Table 5
Objects in Upper Scorpius Observed as Part of the Pulsation Campaign

Object	Telescope	*i*	*J*	SpT	Reference
DENIS-P-J161050.0-221251.6	CTIO 1.0 m	···	12.80	M5.5	1
UScoJ16111705-2213088	CTIO 1.0 m	···	11.64	M5	2
SCH J16111711-22171749	CTIO 1.0 m	17.97	14.34	M7.5	3
UScoJ16113470-2219443	CTIO 1.0 m	···	13.24	M5.75	2
UScoJ16113784-2210275	CTIO 1.0 m	···	11.07	M4	2
SCH J16115737-22150691	CTIO 1.0 m	16.70	13.73	M5	3
SCH J16130306-19293234	P60	16.75	13.45	M5.5	3
SCH J16132809-19245288	P60	16.16	12.92	M6	3
SCH J16172504-23503799	CTIO 1.0 m	17.20	13.74	M5	3
SCH J16173105-20504715	P60	16.49	13.03	M7	3
SCH J16174540-23533618	CTIO 1.0 m	17.44	14.05	M6	3
SCH J16181567-23470847	CTIO 1.0 m	16.18	12.42	M5.5	3
SCH J16182501-23381068	CTIO 1.0 m	17.19	13.72	M5	3
SCH J16183144-24195229	P60	17.76	14.15	M6.5	3
SCH J16183620-24253332	P60	14.75	12.03	M4	3
SCH J16185038-24243205	P60	16.79	13.63	M5	3

Notes. References: (1) Martín et al. (2004); (2) Lodieu et al. (2011); (3) Slesnick et al. (2008)

Observations took place from 2011 January 29 to February 4, for just over seven hours of each day. Although *HST* is a space observatory, the Sun position and other observing constraints resulted in each block of observations ("visit") beginning at roughly the same time every day. Unfortunately much of visit 5 was compromised since the gyroscopic system failed and the field was lost for a number of hours. The viewing limits of *HST* are such that IC 348 objects may be observed for only 46 minutes of each 97 minute orbit. Therefore we designed exposure times to acquire as many images as possible per orbit, without exceeding the telescope's maximum data downlink rate. These varied among 128, 171, and 192 s. All observations were carried out through the F814W filter, which is centered near 8030 Å and similar to *I* band.

HST/WFC3 data are processed by pipeline, which includes standard bias and flatfield calibration, as well as cosmic ray rejection. The MultiDrizzle program corrects for geometric distortion and optimally combines sets of three of four consecutive images, even for undithered data such as ours.

4. PHOTOMETRY ROUTINES

We performed aperture photometry on our target objects using a variety of aperture sizes and sky annulus widths and radii for background subtraction. Different approaches were chosen to produce ground and space-based photometry. For the P60 and CTIO 1.0 m data, we employed a variable-aperture method to optimize flux measurements in a variety of seeing conditions; see Cody & Hillenbrand (2010) for a description of this technique. Both standard aperture photometry and image subtraction algorithms were tested. Typical apertures were 1–2 times the full width at half maximum (FWHM) PSF size, depending on object brightness, and sky annulus radii from 4.5–6 times the FWHM were used to subtract background. To locate photometric nonvariable reference stars, we identified suitable field objects. Typically, we found at least three to four references with photometric stability of several millimagnitudes over the full duration of each run.

For the *HST*/WFC3 images, apertures were fixed for each target and several different sizes were tested, from 2 to 8 pixel, as were sky annulus radii from 8 to 12 pixels and 11 to 16 pixels. Although results did not differ much, the best rms

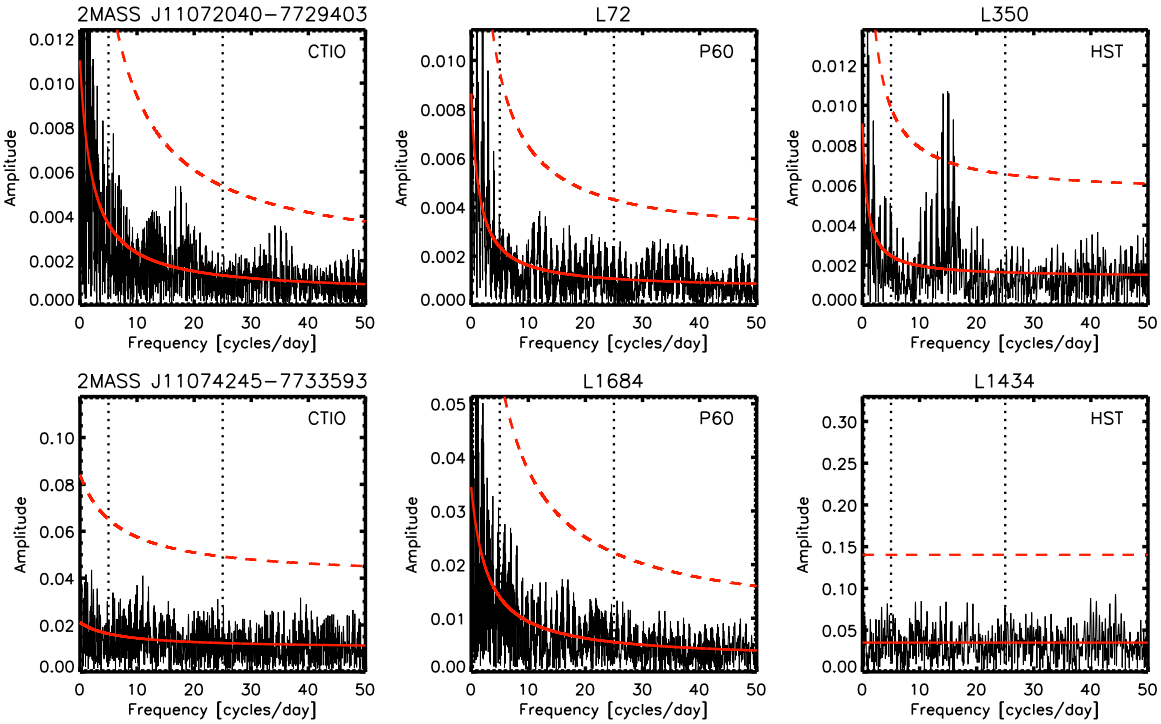

Figure 3. Example periodograms for bright (top row) and faint objects (bottom row), for data acquired from each telescope involved in the pulsation search. Vertical dashed lines indicated the region of frequency space (∼5–25 cd^{-1}) where pulsation is predicted. Solid red curves mark $1/f$ profile fits to the noise level. The upward trends toward low frequency are generally due to intrinsic variability on >1 day timescales. Dashed red curves are four times the noise level, which is our adopted limit for detection of significant signals. The prominent set of peaks between 10 and 20 cd^{-1} in the periodogram of L350 are aliases due to the 97 minute orbital period of *HST*.

(A color version of this figure is available in the online journal.)

light curve values were attained with the 6 pixel aperture and the sky annulus extending from 11 to 16 pixel. Although the Poisson errors are close to 0.001 mag for several targets, the measured RMS light curve spreads are an order of magnitude larger, regardless of the type of photometry employed. This discrepancy suggests that the BDs and VLMSs observed with *HST* are all intrinsically variable.

The light curves produced for all fields were exclusively differential, since our primary interest in short-term flux variations makes photometric zero points irrelevant. By eye, the resulting time series from all telescopes display copious periodic and erratic variability, the latter of which is likely associated with accretion and circumstellar processes (see CH10 and the Appendix). To evaluate the performance of our photometric routines, we omitted variables with rms values of more than three standard deviations above the median trend as a function of magnitude. Careful attention to ground-based reduction procedures enabled us to reach a floor of several millimagnitude photometry at the bright end, comparable to the performance from the space observatories. In general, signal-to-noise, and hence photometric performance, decreased into the BD regime. We provide details on the data quality for individual clusters below in Section 5.

The final light curves were cleansed of artificial variability caused by, e.g., crossings of bad pixel columns and detector malfunctions. In the case of Cha I, a number of reference stars were unavailable on the first night of the run, since the two bottom quadrants of the Y4KCam CCD had failed. Not counting the first night, most Cha I light curves had 278 datapoints for the entire run. To recover additional photometry on the first night for stars in the top of the FOV, we performed image subtraction, which does not rely on reference stars. This resulted in an additional 26 datapoints for about half the targets. Light curves for the other clusters contained between 31 and 528 points.

5. PERIODIC VARIABILITY CHARACTERIZATION

Our main aim in analyzing the light curves of low-mass cluster members was to search for periodicities on the one to four hour timescales predicted for deuterium-burning instability. We produced Fourier transform periodograms (Deeming 1975), which display the amplitude of periodic signals as a function of frequency in units of cycles per day (cd^{-1}), along with the spectrum of noise in the light curve. Examples are displayed in Figure 3. We find that most display an exponential rise toward low frequencies, indicative of systematic effects (both night-to-night photometry shifts and intrinsic aperiodic stellar variability) on >1 day timescales in the light curve. Each periodogram is computed from a lower bound of $1/T$, where T is the total duration of observations, up to the Nyquist limit, or one half of the sampling rate (typically ∼70 cd^{-1}).

True periodicities appear as localized peaks in the periodogram, and we identify them as statistically significant if they rise higher than a factor of 4.0 times the surrounding local noise level (see CH10 for further discussion on this requirement). We determine the noise profile by fitting a curve of form $A/(f + B) + C$ curve to the periodogram values as a function of frequency, f, with constants A, B, and C. This is displayed as the red curves in Figure 3 and confirms that the minimum detectable variability level at low frequencies is somewhat larger than amplitudes observable at higher frequencies (i.e., shorter timescales).

We searched for periodicities in the periodograms corresponding to each light curve, paying particular attention to the 5–25 cd^{-1} range (i.e., periods of 1–4.8 hr) predicted for deuterium burning pulsation. If a period was found, we then removed the best-fit trend (based on multi-sine fits with the program Period04; Lenz & Breger 2005) to produce a pre-whitened light curve. The search for few-hour periodicities was then carried out on this residual.

All targets were subjected to periodogram analysis. As a separate exercise, aperiodic variables were also identified; these "contaminants" are discussed in the Appendix. In the following sections, we describe the results of our period searches in each of the σ Orionis, Cha I, IC 348, and Upper Scorpius regions.

5.1. σ Orionis

With two nearly two-week observing campaigns on the CTIO 1.0 m telescope, we monitored over 150 VLMSs and BDs in the σ Orionis cluster. As detailed in CH10, we identified 38 periodically variable confirmed cluster members, along with 27 periodically variable candidate members. However, all but one of these variables had periods greater than 8 hr. The remaining single object (2MASS J05382570248370) had a period of 7.2 hr. This lack of detections in the one to four hour range was despite sensitivity to periods as short as 15 minutes, and amplitudes as low as several millimagnitudes down to a magnitude of $I = 17$ (and as low as 1 mmag at $I = 14$). We therefore concluded that there are no signs of deuterium-burning pulsation in our σ Ori data set. The full compilation of periodic variables, their phased light curves, and discussion of detection limits appears in CH10.

5.2. Chamaeleon I

Using data from the CTIO 1.0 m telescope, we produced and analyzed light curves for all 32 observed BD and VLMS members of the Cha I cluster. In the interest of fully mining the data set and potentially identifying new cluster members, we additionally performed photometry on all 1548 objects in the Cha I field that were bright enough for detection in individual Y4KCam images ($i \lesssim 22$).

These additional light curves enabled an assessment of the photometric noise as a function of magnitude, as shown in Figure 4. We have fit a trend to the cluster nonmembers, based on the expectations for Poisson and sky noise. Using the fit values as an indication of the magnitude-dependent photometric uncertainty, we have then selected variable objects via the χ^2 test. The full collection of these light curves is presented and discussed in the Appendix. The floor of the rms distribution reaches ~3 mmag at an I-band magnitude of 14, as shown in Figure 4. Objects with $I < 17$ display a photometric precision of 1% or better.

For each object in the sample, we carefully analyzed the periodograms for signs of periodicities on the few-hour timescales predicted for D-burning pulsation. Among the known cluster members, only four stars have estimated masses above ~0.4 $M_\odot$, and so most are candidates for the instability.

Based on the observing cadence of 600 s, we are sensitive to periodic signals with frequencies as high as 72 cd^{-1} (i.e., $P =$ 20 minutes). The majority of light curves contain low-frequency variations, most of which are due to intrinsic erratic variability; these shape the exponential rise in periodogram amplitude at $<1\ cd^{-1}$. Despite sensitivity to few-millimagnitude levels, we do not find any evidence for variability with periods less than 16 hr, apart from one field object that appears to be a main sequence pulsator.[4] A few periodograms display low-level signals in the range where pulsation is expected, but none of these meet the 99% significance level criteria, and we find most to be aperiodic variables. Furthermore, the light curves do not show clean trends when phased to these periods. We conclude that none of the 32 very-low-mass objects in the Cha I sample are periodic on one to five hour timescales, at least at or above the amplitude levels probed by the data.

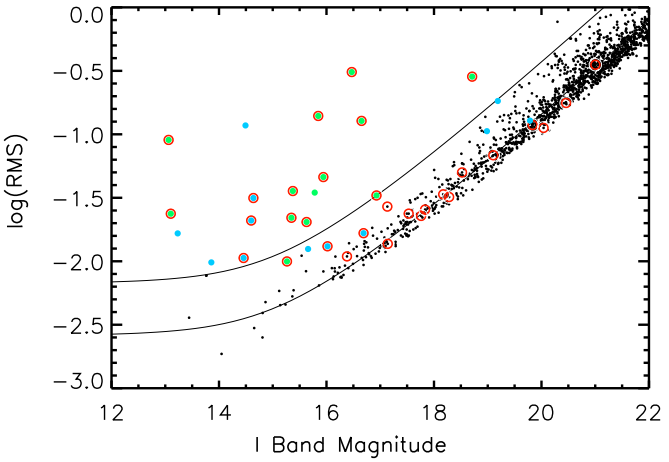

Figure 4. RMS spread of light curves over the 13-night duration of the Cha I observations, for periodic (blue) and aperiodic (green) variables. Confirmed cluster members appear as red circles. We plot the estimated total contributions from Poisson, mean sky level, and systematic noise, shifted upward by 0.24 dex so as to match the median of the data (lower solid line). The curve corresponding to 99% probability of variability detection via the χ^2 test appears above this.

(A color version of this figure is available in the online journal.)

On longer timescales, the final sample of variables contains 12 periodic objects in Cha I with clear variability. Observed and phased light curves for the cluster members among these are presented in Figure 5. We also identified periodic behavior among eight additional objects of unknown membership status. In most of these cases, the light curve shapes are characteristic of field pulsators or eclipsing binaries, and blue colors suggest locations in the background field. However, two relatively red objects with sinusoidal light curves may be bona fide Cha I members (2MASS J11073302−7728277 and 2MASS J11122675−7735183). The former (also known as CHXR 25) was classified by Luhman (2007) as a field dwarf, while the latter has no previous literature and would benefit from spectroscopic follow-up. The light curves for these new Cha I candidates are presented in Figure 6.

The measured properties for all variable sources in Cha I are listed in Table 6. This includes the aperiodic variables uncovered with the χ^2 test, as discussed in the Appendix. Of note, few Cha I members have been photometrically monitored previously, apart from a sample of 10 BDs and VLMSs presented by Joergens et al. (2003). Of the five with periods reported in that work, *none* are redetected as periodic variables here.

5.3. IC 348

In IC 348 the photometry includes only known cluster members, since high extinction in the region blocks our view of most background field stars. We were therefore unable to perform a full assessment of photometric precision based on

[4] The star 2MASS J11105665−7733557 has a period of 3.3 hr and amplitude 0.12 magnitudes in the I band. However, its near-infrared colors lie well blueward of the young cluster sequence, implying that it is not a Cha I member.

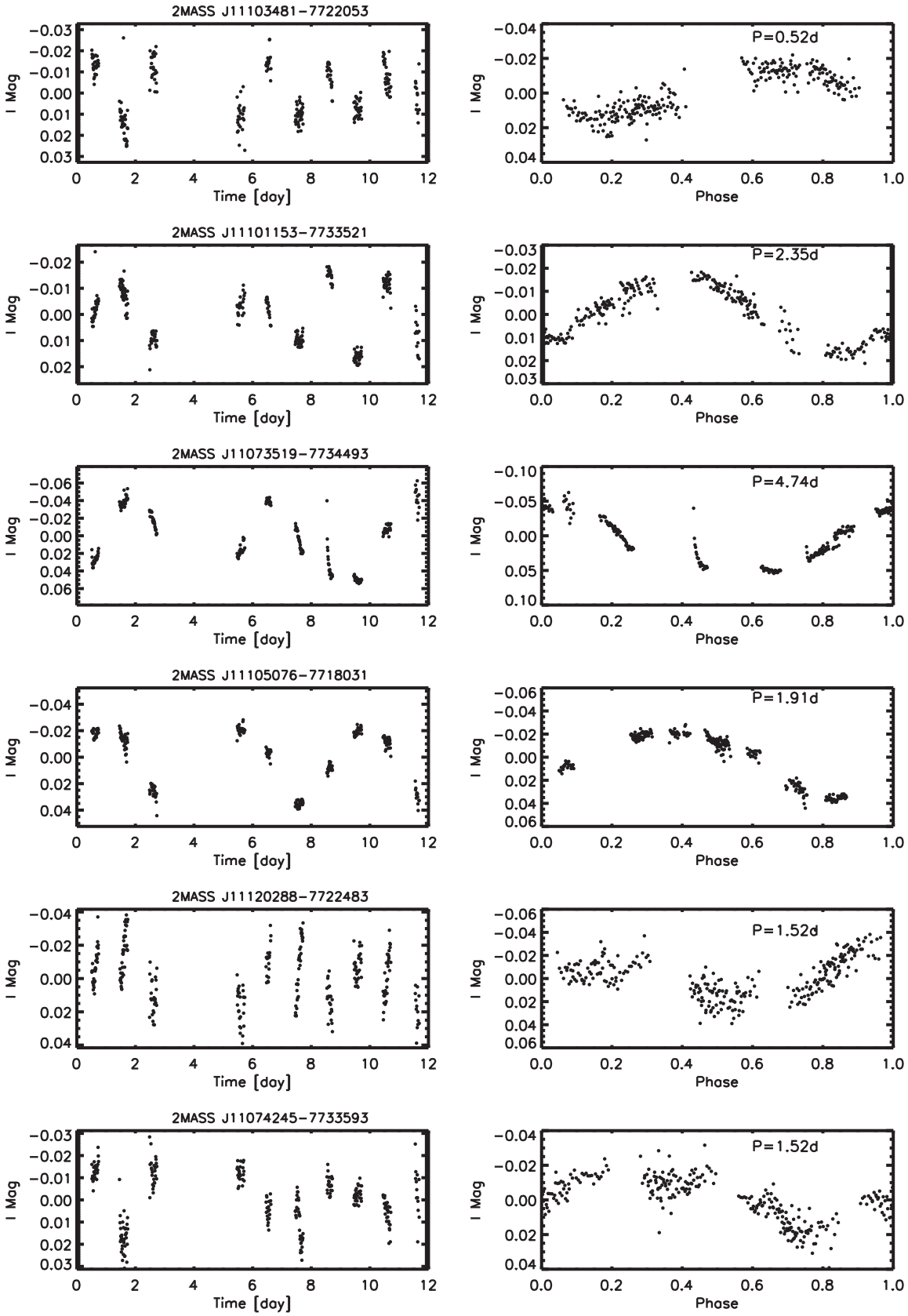

Figure 5. Differential light curves for very-low-mass Cha I members with detected periodic variability. The first column shows the original light curve, while the second is the light curve phased to the detected period.

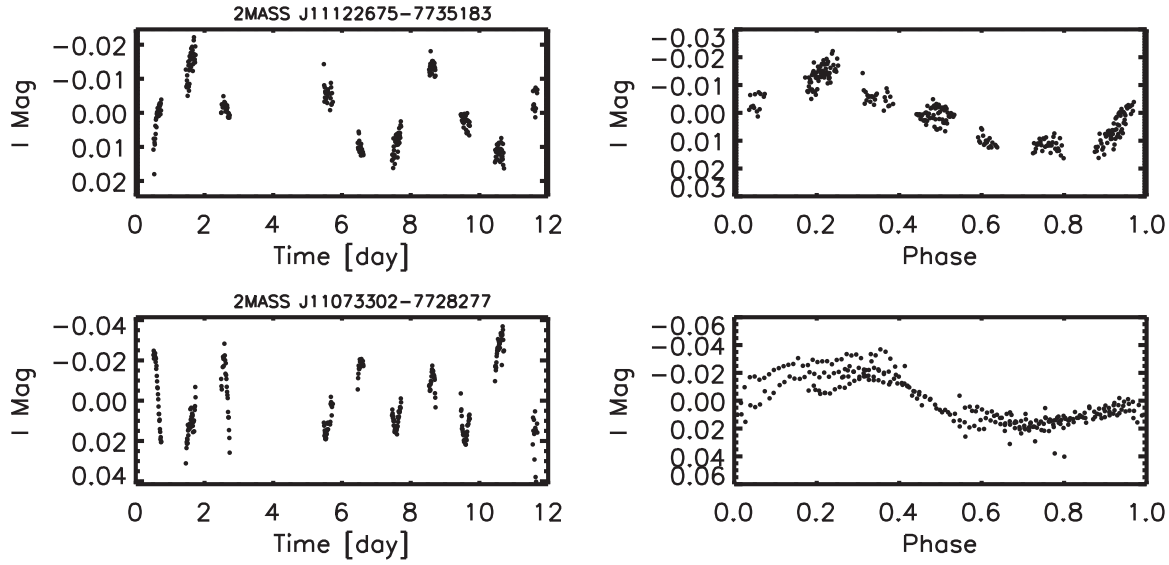

Figure 6. Light curves for new candidate Cha I members with detected periodic variability. The first column shows the original light curve, while the second is the light curve phased to the detected period.

Table 6
Cha I Objects with Detected Variability

Object	Variability Type	Period	Amplitude	RMS	Disk?	Member?
2MASS J11065906-7718535	A	···	0.405	0.090	Y	Y
2MASS J11071668-7735532	A	···	0.405	0.090	Y	Y
2MASS J11072040-7729403	A	···	0.105	0.022	N	Y
2MASS J11072988-7725017	P	2.28d	0.25	0.117	···	N
2MASS J11073302-7728277	P	0.67d	0.0197	0.017	N	M
2MASS J11073519-7734493	P	4.74d	0.0478	0.031	N	Y
2MASS J11073686-7733335	A		0.098	0.020	N	Y
2MASS J11074245-7733593	P	1.52d	0.0138	0.012	···	N
2MASS J11075225-7736569	A	···	0.090	0.022	N	Y
2MASS J11082238-7730277	A	···	0.229	0.046	Y	Y
2MASS J11083952-7734166	A	···	0.145	0.036	Y	Y
2MASS J11085421-7732115	A	···	0.043	0.010	N	Y
CTIO J11093360-7731113	P	0.46d	0.1271	0.128	···	N
2MASS J11094742-7726290	A	···	0.571	0.128	Y	Y
2MASS J11094918-7731197	A	···	0.128	0.026	N	Y
2MASS J11101153-7733521	P	2.354d	0.0152	0.011	N	Y
2MASS J11103481-7722053	P	0.5229	0.0137	0.013	N	Y
2MASS J11105076-7718031	P	1.91d	0.0286	0.021	N	Y
2MASS J11105359-7725004	A	···	1.431	0.285	Y	Y
2MASS J11105665-7733557	P	0.14d	0.1244	0.106	···	N
CTIO J11111463-7737020	P	0.59d	0.1827	0.183	···	N
2MASS J11120288-7722483	P	1.52d	0.0169	0.017	N	Y
2MASS J11120351-7726009	A	···	1.122	0.309	Y	Y
2MASS J11122675-7735183	P	3.52d	0.0129	0.010	N	M
2MASS J11122971-7731045	A	···	0.171	0.035	···	M

Notes. We list objects in the Cha I field with detected variability. "A" corresponds to aperiodic variability, while "P" is for periodic variability. The values listed in Column 4 are either the half amplitude for periodic sources or the peak-to-peak amplitude for aperiodic sources. In Column 5 we provide the rms light curve spreads in *I*-band magnitudes. The disk column indicates whether mid-infrared *Spitzer* data exhibits an excess; "−" indicates a lack of *Spitzer* photometry. Membership is based on previous censuses of Cha I; nonmembers ("N") have colors that are inconsistent with a position above the main sequence. "M" indicates a possible new cluster member based on the detected variability.

nonvariable field stars. However, a plot of rms light curves values versus magnitude (shown in Figure 7) provides a rough estimate of the performance for our P60 data set. Over the course of a single night, we reach a precision of ∼2 mmag at $I = 13$, and better than 0.01 mag down to $I \sim 17$. The rms values measured over the entire week-long duration of the light curves show considerably higher spreads in photometry, ∼1% or higher in most light curves. We attribute much of this to intrinsic variation of the stars on >1 day timescales.

We performed a period search analysis on all IC 348 cluster members observed with the P60 and *HST*. For the former, we are sensitive to periodicities on timescales from approximately 9 minutes to 12 days (resulting from a cadence of 270 s). Since we did not obtain data every night, our sensitivity to periods

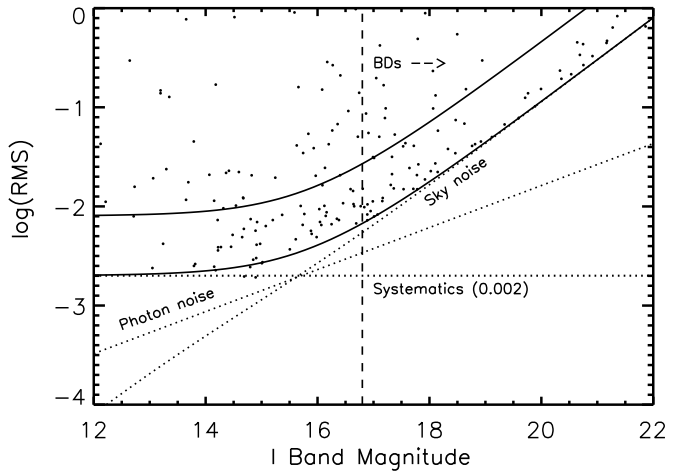

Figure 7. RMS spread of light curves for sources in IC 348, as measured over the course of a single night. All plotted objects are confirmed cluster members. We show the estimated total contributions (solid line) from Poisson, mean sky level, and systematic noise. The upper solid curve corresponds to an estimate for 99% probability of variability detection. There is no clear boundary between variable and nonvariable sources here, unlike in Figure 4, which contains a mix of young cluster members and field stars.

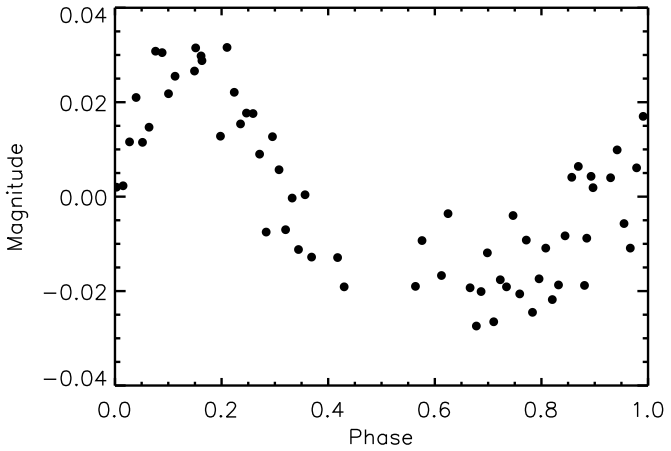

Figure 8. Phased light curve of the IC 348 object L761, observed with *HST*/WFC3. This BD displays significant periodic variability on a timescale of 0.6 days.

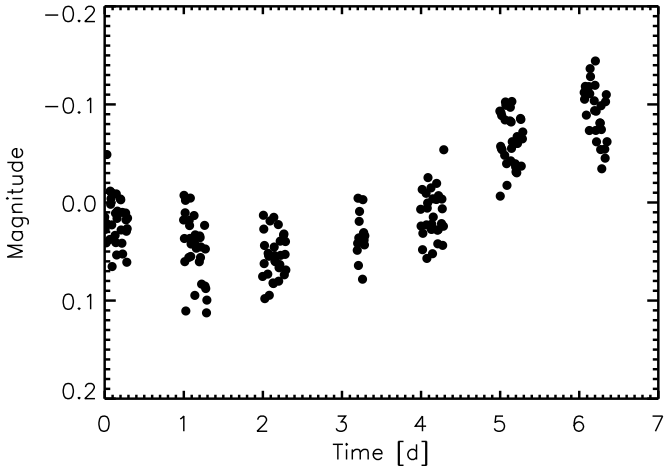

Figure 9. Light curve of the IC 348 object L1434, observed with *HST*/WFC3. This BD displays significant variability over the seven days that it was monitored.

of more than a few days is highly nonuniform. We therefore focused on the short periods predicted for D-burning pulsation.

We generated periodograms from the light curves of all 147 unsaturated objects in the ground-based P60 field, including 91 BDs and VLMSs. A large fraction of these display variability by eye, much of which is erratic and dominated by low-frequency behavior. It is thus not surprising that many of the periodograms display excess power around 5–10 cd^{-1}, which we attribute to aliasing, based on the window function, which shows a series of peaks centered around 8 cd^{-1}. Further support for the spurious nature of these signals is that they do not reach the 99% significance level, and no coherent periodicity emerges when the light curve is phased.

In some cases, an obvious and statistically significant periodicity did appear on timescales of one day or more, suggesting rotation. When this occurred, we fit the overall trend and removed it from the light curve before searching for shorter timescale pulsation signals. In *none* of the IC 348 light curves did we uncover significant periodicities on the 1–5 hr timescales indicative of pulsation.

Similar to the ground-based monitoring data, the *HST* time series are subject to aliasing. This effect is associated with the 97-minute orbital timescales and is seen prominently in the periodogram of object L350, shown in Figure 3. Omitting the frequency regions subject to aliasing, we have again searched for periodicities on one to five hour timescales, in hopes of detecting pulsation. In general, we find that the periodogram values are consistent with noise at the 1–5 mmag level in the frequency range of interest (5–25 cd^{-1}).

Two exceptions in the *HST* data set are the IC 348 BDs L761 and L1434. The former is periodically variable, as shown in Figure 8. The period of 0.6 days is consistent with rotational modulation by one or more spots on its surface. L1434 is also variable (see Figure 9), but we are unable to determine whether it is periodic without a longer duration data set.

5.4. Upper Scorpius

As with the other young star regions, we produced discrete Fourier transforms to search for periodicities on a variety of timescales in Upper Scorpius. Targets here were observed during a number of runs (see Table 1), and we are sensitive to periodicities as short as 10 minutes in each of these data sets. The longest period detectable varies with the length of each observing run and ranges from less than 2 days to 16 days. Since some of the runs only had six or fewer total nights, the associated periodograms have lower frequency resolution than the data sets on other clusters, and the search for periodicities is more susceptible to systematic effects. While some of the objects display variability on night-to-night timescales, we cannot accurately quantify all possible periodicities. We therefore focused exclusively on the search for pulsation at one to five hour periods. Detection of signals in this period range is feasible given the number of datapoints (30–550, depending on the run) and the fairly low photometric uncertainties of the BDs (1%–3%).

We find that the data generally have sensitivity to signals in the few millimagnitude to 0.01 mag amplitude range. Despite this, none of the objects in USco showed significant periodic variability. However, the light curves of a few displayed night-to-night variations that may be indicative of accretion or variable circumstellar extinction.

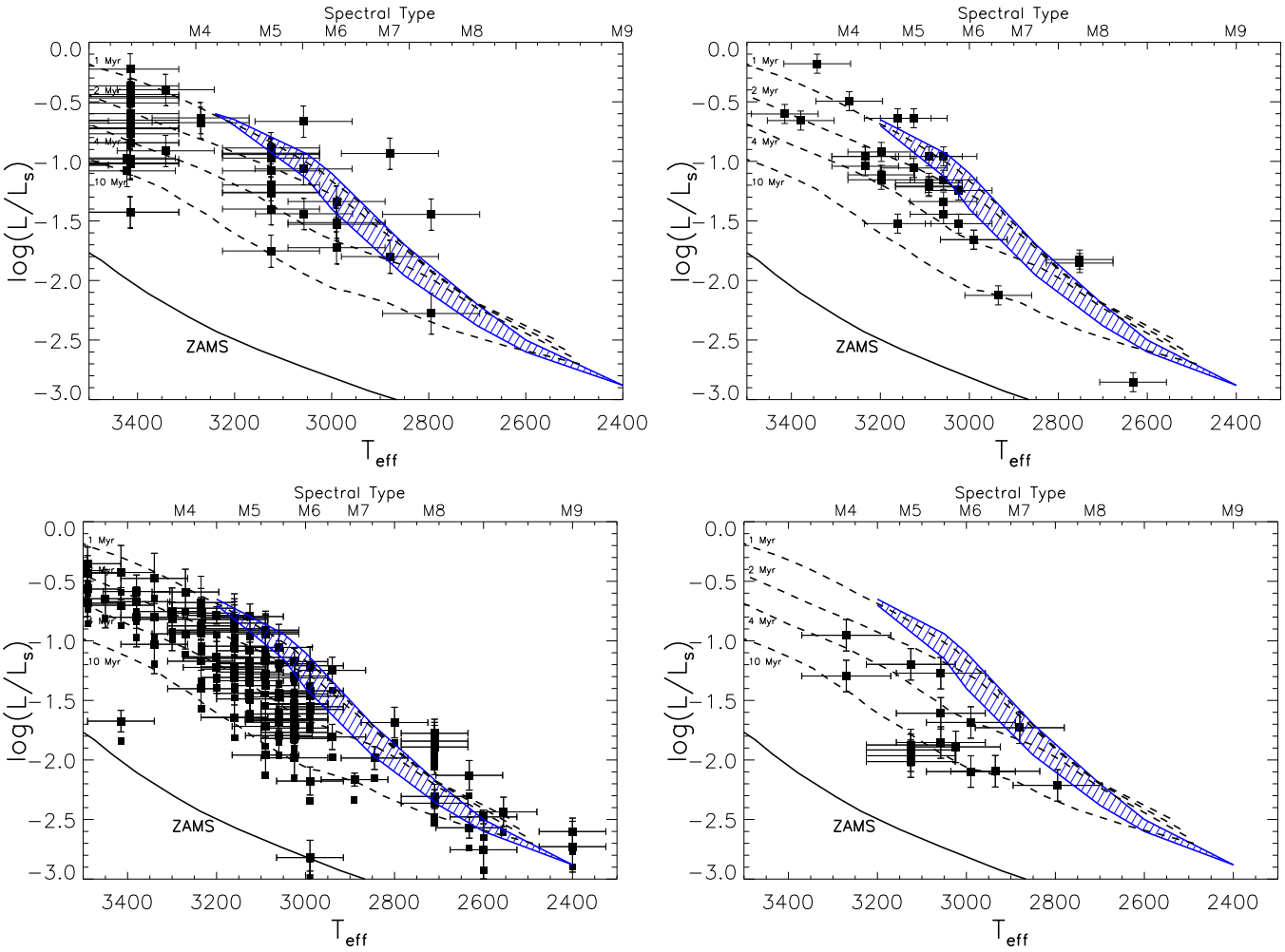

Figure 10. We plot young cluster members on the H-R diagram, along with the deuterium-burning instability strip from PB05 (blue dashed region). Isochrones are from Baraffe et al. (2003), and L_S is the solar luminosity. At upper left is σ Orionis, with an assumed distance of 440 pc; at upper right is Cha I ($d \sim 160$ pc). At lower left is IC 348, with an assumed distance of 316 pc; at lower right is Upper Scorpius ($d \sim 145$ pc). Many of the observed objects appear to lie directly on the strip, and many others have a non-negligible probability of lying on it given their H-R diagram errors.

(A color version of this figure is available in the online journal.)

6. NONDETECTION OF THE DEUTERIUM BURNING INSTABILITY

With no periodicities observed in the one to four hour range for any of the clusters monitored, we now consider the implications of our nondetections. In each region, we assess the set of temperatures and luminosities in relation to the deuterium burning instability strip on the H-R diagram. The number of objects on or near the theoretically predicted region then sets the probability of detection, or lack thereof.

In σ Orionis, our search for signs of deuterium burning oscillations among members was carried out with the CTIO 1.0 m and *Spitzer* telescopes, as detailed in Cody & Hillenbrand (2010) and Cody & Hillenbrand (2011), respectively. Within the uncertainties of cluster membership verification, there were approximately 40 objects with masses less than $\sim$0.1 $M_\odot$. Of these, of order 15 had temperatures and luminosities overlapping the instability strip. We present the H-R diagram of observed Ori objects with available spectral types, for a distance of 440 pc, in Figure 10.

Our failure to detect short-period variability in σ Ori is inconsistent with the predictions of PB05, a conclusion we further quantify in the next section. It is also at odds with previous reports of short-period variability in young BDs observed by Bailer-Jones & Mundt (2001) and Zapatero Osorio et al. (2003).

Prior evidence for short-timescale variability was weaker (or nonexistent) in the other three clusters. To assess prospects for pulsation here, we performed the same H-R diagram evaluation as done for σ Ori. In Cha I, four objects in our sample fall squarely on the instability strip when we convert spectral types to temperatures using the scale of Luhman et al. (2003). A further 24 have spectral types later than M4 and therefore may be burning deuterium and subject to pulsation. We plot the full sample of Cha I members in our field on the H-R diagram in Figure 10.

To estimate the number of our IC 348 targets that should be susceptible to the D-burning instability, we have plotted their positions on the H-R diagrams in Figure 10, assuming a distance of 316 pc. Many objects overlap the predicted D-burning pulsation strip. We also present the H-R diagram of observed USco objects in Figure 10. Of the 17 very-low-mass USco members observed, one lies squarely on the instability strip: SCH J16173105−20504715. However, its periodogram does not exhibit any significant signals in the region expected for pulsation.

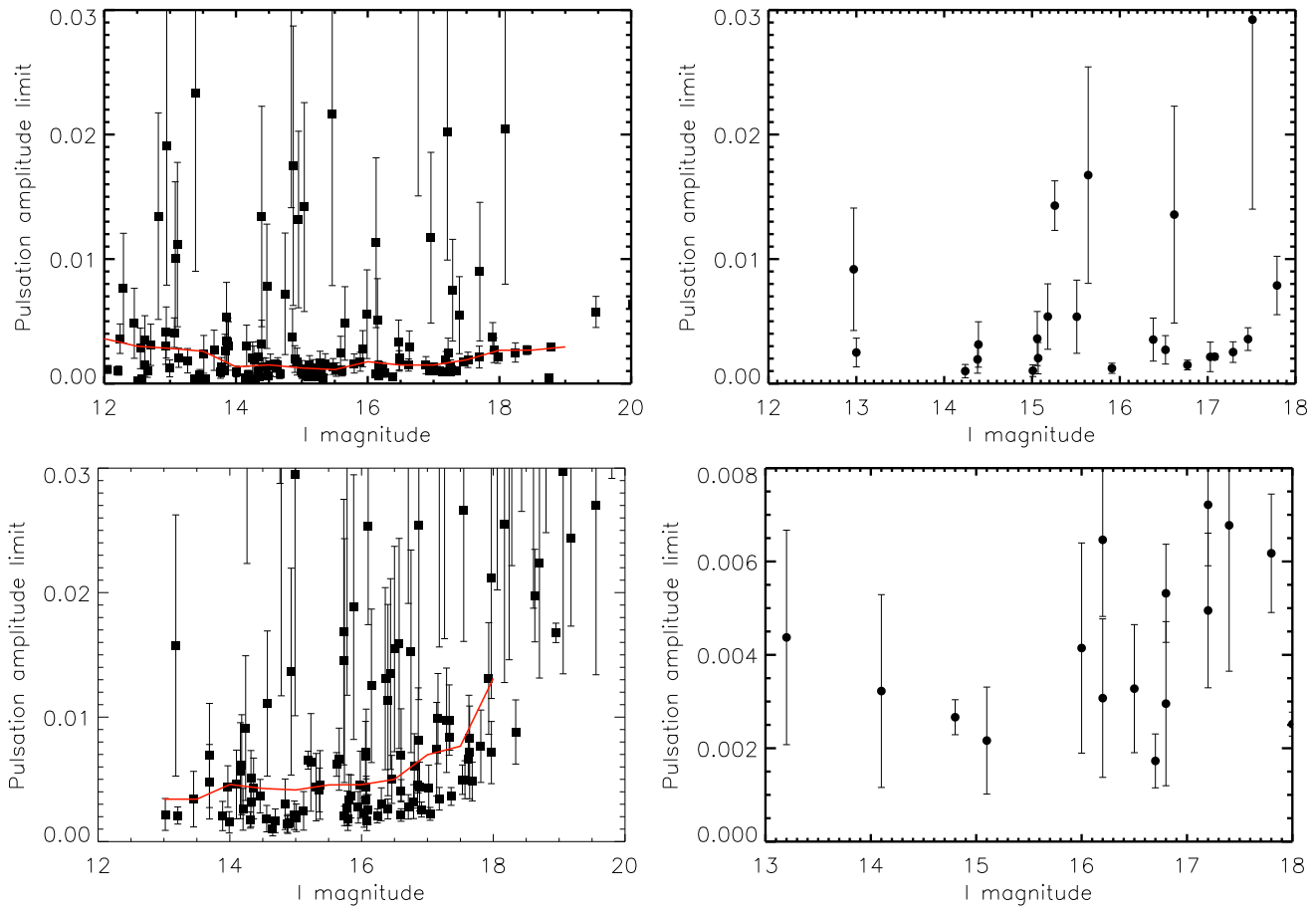

Figure 11. Pulsation detection limits for individual objects vs. their magnitudes. The clusters represented clockwise from the top left: σ Ori, Chamaeleon I, IC 348, and Upper Scorpius. For σ Ori and IC 348, we have drawn a median curve, binned by magnitude, in red. Based on the position of the instability strip, we would expect pulsating objects to have magnitudes of ∼14 and fainter. While in general the limits are quite low—in the millimagnitude range—there is a large population of outliers in which high-amplitude intrinsic aperiodic introduced significant power into the higher frequency regions of the periodogram.

(A color version of this figure is available in the online journal.)

A number of other targets could lie on the strip if their 1σ temperature and luminosity errors are considered, and this is true for each of the clusters examined. Below, we will use these uncertainties to assess the statistic likelihood of failing to observe pulsation in the overall monitoring data set.

6.1. Statistical Evaluation of Pulsation Probabilities

We uncovered many cases of periodic variability in the collected time series, over a wide range of timescales. Our detection of both rotation on ∼1–3 day timescales in young cluster members and variability on hour timescales in background field pulsators and eclipsing binaries shows that our period detection algorithms are robust. Yet in the search for deuterium-burning pulsation, the data unanimously point to one conclusion: this instability is not present in young BDs and VLMSs above an amplitude of several millimagnitudes in the *I* band.

One might argue that objects in our data set simply do not exhibit pulsation because they are not situated on the H-R diagram instability strip. However, the large sample size makes this possibility highly unlikely. To show how improbable the chances are that *none* of our sample have H-R diagram positions overlapping the instability strip, we consider temperature–luminosity probability distributions for each object. We take these to be two-dimensional asymmetric Gaussians, normalized and centered at the adopted luminosities and temperatures. The Gaussian widths are given by the associated 1σ uncertainties, which are shown in the H-R diagrams in Figure 10. The position of each target then corresponds to a probability that it is susceptible to pulsation, which we determine by integrating its distribution over the entire region of the instability strip. For objects on or very close to the strip, this value is at least ∼20%–25%, whereas for the higher mass stars far from the strip it is close to zero. The probability that the position of a given object does *not* overlap with the instability strip is then 1.0 minus this quantity. The product of these values over all targets provides an estimate of the chance that no pulsators would be present in our sample.

We have performed this exercise for each of the clusters observed, and for alternate distances in cases where there is more than one possible value (IC 348 and σ Ori). Since the instability strip runs nearly along isochrones and varies slowly in luminosity, changes in the adopted distance can have a significant impact on the number of objects expected to pulsate. We take all possibilities into consideration.

In Cha I, we determined an expectation value of 3–4 objects on the strip and find a probability of 0.015 that *no* object positions actually overlap it. Turning this number around, there is a nearly 99% chance that at least one object should exhibit pulsation based on its position within the instability strip, assuming that the theoretical calculations underpinning it (PB05) do not suffer from gross systematic errors. Likewise in Cody & Hillenbrand (2011), we found a 70%–80% chance that at least one of our σ Ori targets observed in the infrared with *Spitzer* should exhibit

pulsation. This is in contrast to the lack of short period variability in that data set.

USco does not have many targets overlapping the instability strip, and therefore the expectation is for only 1 or 2 objects to lie directly on it. In this region, we find a non-negligible probability of 0.22 that our sample did not include any pulsation candidates. For IC 348, on the other hand, we expect ∼11 objects on the strip and find a probability of 4×10^{-6} that none are actually on it. This is assuming a distance of 316 pc Herbig (1998). If we instead assume a lower distance of 260 pc based on *Hipparcos* parallaxes (Scholz et al. 1999), then the expectation is similar: nine objects on the strip and a probability of 5×10^{-5} that none are on it.

Finally, we have computed probabilities for σ Ori. The precise number of pulsation candidates depends on the adopted distance, which is debated to be either 350^{+120}_{-90} pc, based on the *Hipparcos* parallax of σ Ori AB, or 440^{+30}_{-30} from main sequence fitting (Sherry et al. 2008). Assuming a cluster distance of 440 pc (Sherry et al. 2008) we find that at least 4 targets are expected to be on the strip, with at most a 0.02 chance that none are. Substituting the alternate distance of 350 pc, we find nearly the same values (3, 0.06). The probabilities are upper limits since we do not have spectral types for part of the σ Ori sample and hence cannot reliably place these objects on the H-R diagram.

In conclusion, we expect with high confidence to have observed deuterium-burning oscillations if it is present at observable amplitudes. We now quantify the overall detection limits by considering the power-law fit to the periodograms of each observed young cluster member. These curves, of form $A/(f+B)+C$ for frequency f and constants A, B, and C, trace out the noise level as a function of frequency (see Figure 3). For each object analyzed, we take the fit values at 5 cd^{-1} (∼5 hr) and 25 cd^{-1} (∼1 hr) as representative of the 1σ level above which no pulsation is observed. We display these values as a function of object magnitude in Figure 11 to illustrate the collective limit imposed by our entire data set.

The median amplitude limit is several millimagnitudes. Objects with high-amplitude aperiodic variability (see the Appendix) are exceptions, as they have excess periodogram noise which is intrinsic. The rest of our targets, however, have maximum amplitudes in the periodogram of at most 0.002–0.004 mag. This represents the threshold above which we detect no periodicities. We conclude that if deuterium-burning pulsation is present in any of our sources, then its amplitude must be below this level.

7. CONCLUSION

Despite exquisite photometric sensitivity, we have not detected signs of short-period variations in any of our young BD and VLMS targets. Although the theory of PB05 does not preclude very low amplitudes, we suspect that the failure to find pulsation is indicative of a physical damping mechanism operating within these objects. The convective timescale is over two orders of magnitude longer than the pulsation timescale, but it becomes quite short near the (sub)stellar surface layers. Neglect of the energy exchange between pulsation and convection may have led to overly optimistic predictions of mode amplitude growth. Indeed, models of this interaction in other types of stars have recently shown that convection can quench pulsation under some circumstances (Gastine & Dintrans 2011).

To continue the search for pulsation and probe to lower amplitudes, future campaigns will need to produce extraordinarily high precision photometry. Data of this quality is available through the *CoRoT* mission, but only for stars brighter than ∼15th magnitude in the optical in the NGC 2264 cluster. K2, the successor mission to *Kepler* shows further promise as it will provide exquisite monitoring on hundreds of Upper Scorpius members.

Based on observations made with the NASA/ESA *Hubble Space Telescope*, obtained at the Space Telescope Science Institute, which is operated by the Association of Universities for Research in Astronomy, Inc., under NASA contract NAS 5-26555. These observations are associated with program 11610. A.M.C. thanks the CTIO Telescope Operations staff for help in carrying out observations. Observation time on SMARTS consortium facilities was awarded through the National Optical Astronomy Observatory, operated by the Association of Universities for Research in Astronomy, under contract with the National Science Foundation.

APPENDIX

CONTAMINATION BY APERIODIC VARIABILITY

In searching for periodicities among our young cluster targets, we encountered a number of light curves with rms values well above the median for field objects of similar magnitude. This aperiodic variability introduces low-frequency noise into the periodograms and raises the threshold over which we can detect pulsation signals. While this behavior may "contaminate" the pulsation search, it is interesting in its own right, as it offers insights into accretion and disk properties. We have assembled a collection of aperiodic variables in each of the clusters apart from USco, which did not have a sufficient sample size to mine non-periodic variables.

In general, we used plots of light curve rms versus magnitude (e.g., Figures 4 and 7) to select objects with variability at the 99% confidence level (see CH10 Section 6 for a full description of detection procedures). In σ Ori we uncovered 42 aperiodic variables with amplitudes from a few percent up to a full magnitude. Combining these with the periodically variable objects in that cluster, we found a total variable fraction of 69% for σ Ori members (CH10).

Using the same detection approach in the Cha I field, we found 13 aperiodic variables, all but one of which are confirmed cluster members. The remaining object, 2MASS J11122971−7731045, has peak-to-peak variations of just over 0.1 mag in the *I* band. We provide the list of aperiodic variables in Table 6, and show their rms values in Figure 4. Their light curves are provided in Figure 12. Of note, three stars previously listed as periodic (Joergens et al. 2003) appear to be aperiodic, since they are detected as variable based on light curve rms but do not show distinct signals in their periodograms. These are 2MASS J11085421−7732115 (CHXR 78C), 2MASS J11075225−7736569 (Cha Hα 3), and 2MASS J11083952−7734166 (Cha Hα 6).

In the Cha I sample, the total variability fraction (including periodic objects) is between 53% and 69%, depending on the membership status of several newly identified variable stars. This is statistically comparable to the fraction found in σ Ori (CH10). The Cha I variability classification is divided into roughly equal proportions of periodic and aperiodic objects. Among the eight variables with no prior membership information, five have light curves and colors characteristic of field eclipsing binaries

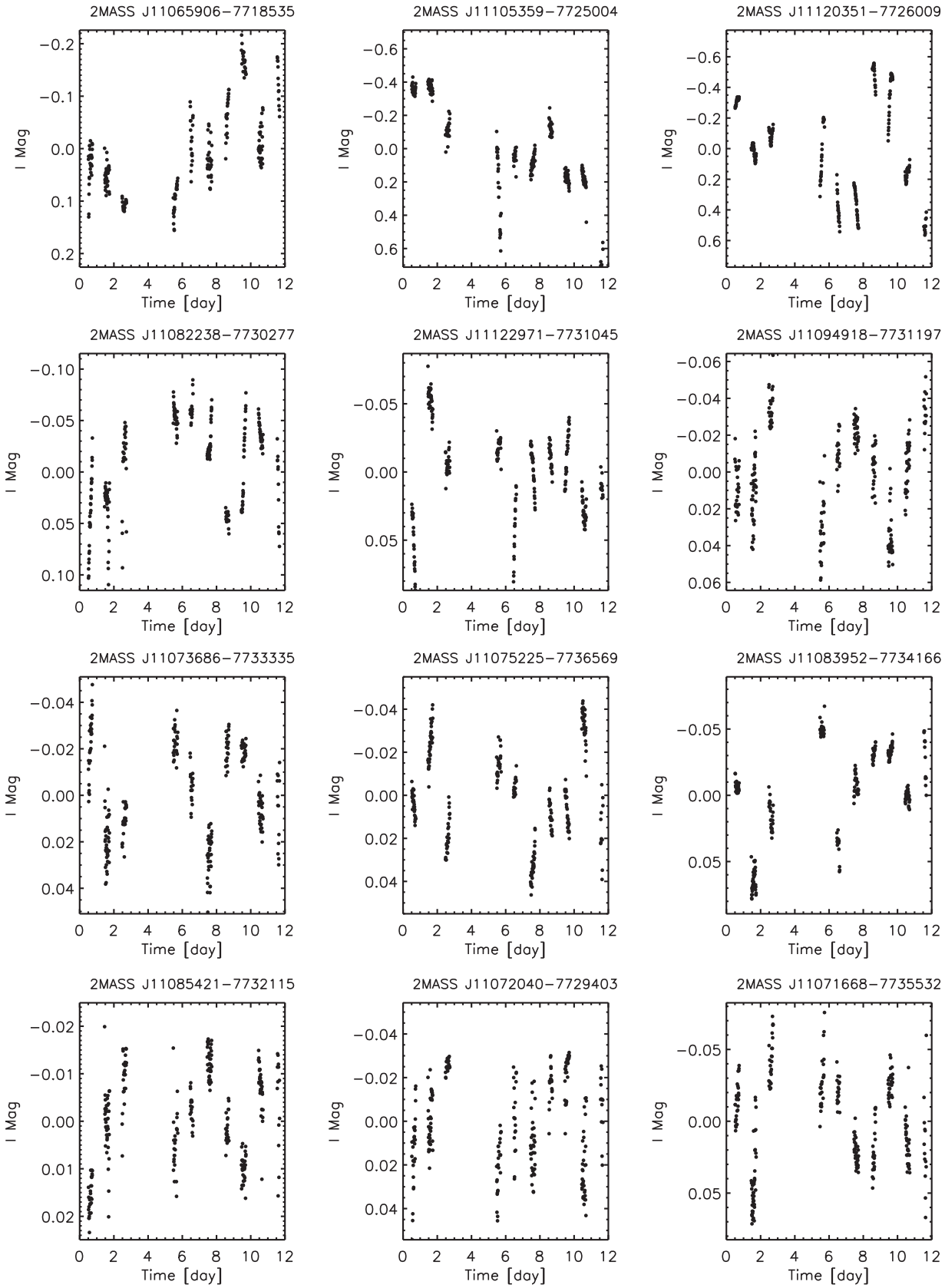

Figure 12. Light curves of very-low-mass Cha I members selected as aperiodic based on large χ^2 values and lack of periodicities. Membership information is available in Table 6; 2MASS J11122971−7731045 is a new Cha I candidate.

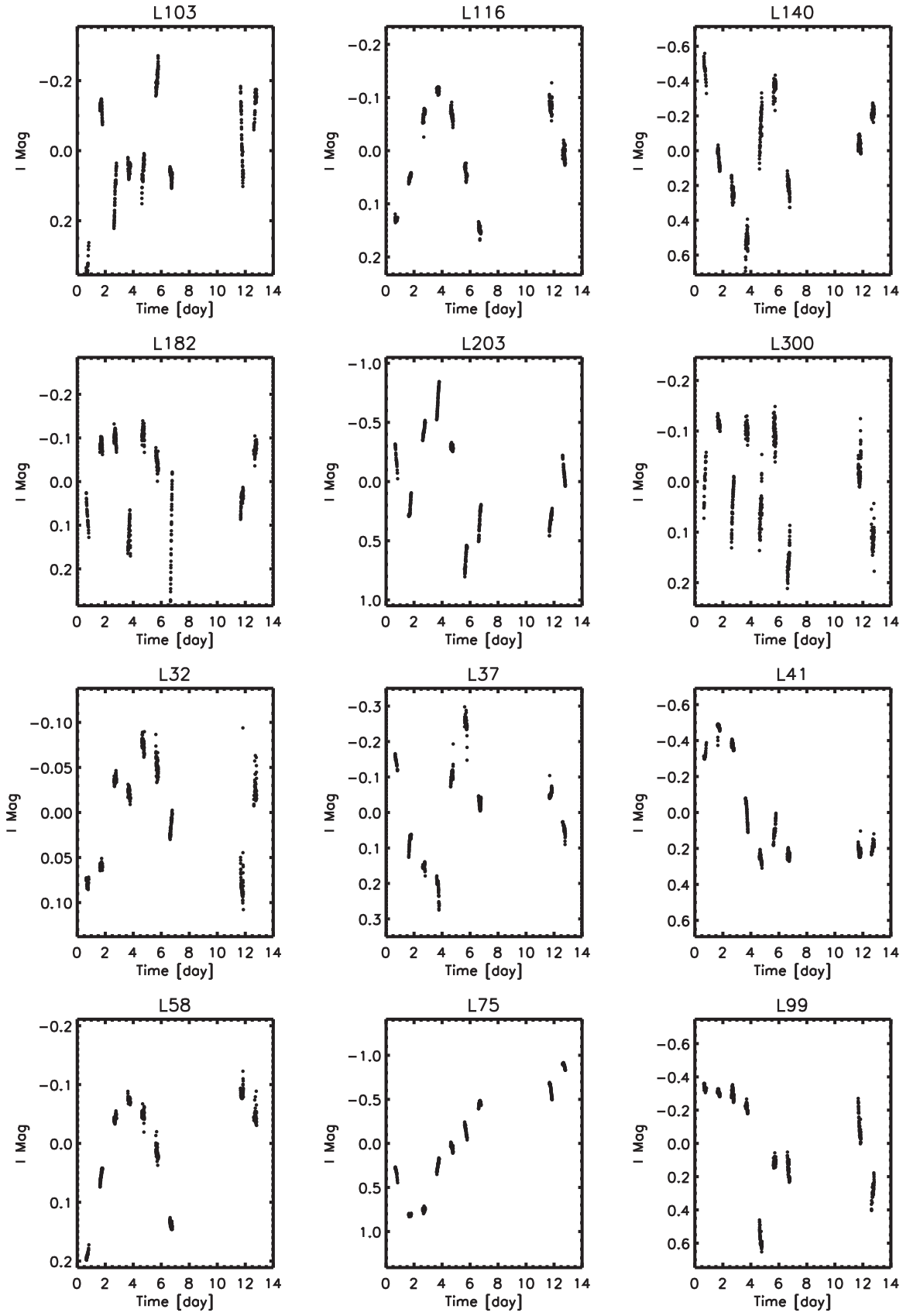

Figure 13. Light curves of IC 348 members selected by eye as being prominent variables. Ids are as in Table 3.

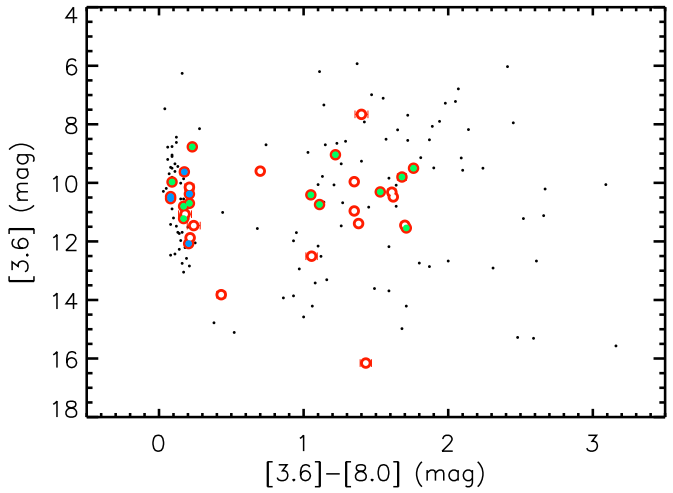

Figure 14. *Spitzer* photometry of likely Cha I members. Objects found in our photometric sample are marked with red circles, while those out of the fields are left as dots. Error bars are included but in many cases too small to see. Aperiodic variables detected in our photometry are overplotted as filled green circles, while periodic variables in our sample are marked by filled blue circles. The nearly vertical cluster of objects near [3.6]–[8.0] = 0 is the sequence of colors and magnitudes pertaining to bare photospheres.

(A color version of this figure is available in the online journal.)

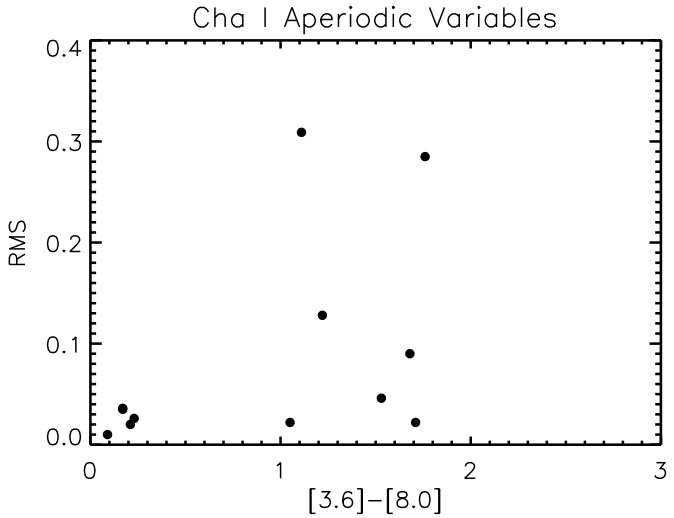

Figure 15. *Spitzer* [3.6]–[8.0] color vs. light curve *I*-band rms value for our aperiodic variables in Cha I.

or pulsators. Three may be new members, and we note these in Table 6.

In the IC 348 sample, there were no nonvariable field stars available for determination of the photometric uncertainty as a function of magnitude. As a result, we could not calculate accurate χ^2 values for the light curves from this cluster. However, a rough cutoff for rms values indicative of variability (i.e., upper line in Figure 7) suggests that there are a number high-amplitude variables. We examined the light curves of objects above the upper curve in Figure 7 and removed from consideration those for which artificial systematic effects (i.e., tracking and flatfielding errors) appeared to cause a high RMS. We are left with nine IC 348 objects with strong variability; these light curves are depicted in Figure 13. Their identification numbers, from Luhman et al. (2003), are provided above each panel.

Beyond identification of the aperiodic variables in our data set, we can assess correlations between their flux behavior and the presence of circumstellar disks. We cross-referenced our photometric samples in σ Ori and Cha I with those of Luhman et al. (2008), and Luhman & Muench (2008), which provide *Spitzer* Infrared Array Camera (IRAC; 3.6–8.0 μm) and in some cases Multiband Imaging Photometer for Spitzer (MIPS; 24 μm) photometry. In σ Ori, we find that 133 of 153 confirmed or candidate members in our time series data set have *Spitzer* photometry, including 57 of 65 cluster periodic variables. For the Cha I sample, all 37 cluster members monitored in the *i* band have available IRAC measurements, and in many cases, MIPS data in addition. While there is *Spitzer* data available for the IC 348 cluster as well, we have not included it in the analysis here since extensive comparison of photometric periods with infrared excess was already carried out by Cieza & Baliber (2006). Furthermore, our own IC 348 photometry is difficult to cleanly separate into the periodic and aperiodic categories due to the systematics resulting from the lack of tracking on the P60 telescope.

We display in Figure 14 the distribution of *Spitzer*/IRAC 3.6–8.0 μm colors for all objects in our Cha I data set with available infrared photometry; the equivalent plot for σ Orionis is shown in Figure 13 of CH10. As seen in these diagrams, the samples split relatively cleanly into two groups, with the narrower blue sequence near [3.6]–[8.0] = 0 representing bare photosphere colors. The cloud of objects with [3.6]–[8.0] colors between 1 and 2 is indicative of infrared excesses signifying the presence of a dusty disk. While the sequence of *photospheric* colors is fairly well defined, several ambiguous objects lie between 0.3 and 0.7 mag. We have therefore chosen a somewhat conservative disk selection criteria of [3.6]–[8.0] > 0.7 (e.g., Cieza & Baliber 2007) so as to omit these objects from the disk sample.

In total, we identify 21 disk-bearing Cha I members with both photometry from our campaign and *Spitzer* colors indicative of disks. The resulting disk fraction in our sample is $57 \pm 9\%$. We find that our disk identification is entirely consistent with that of Luhman et al. (2008) and Luhman & Muench (2008) (based on the same *Spitzer* data). The full listing of disk classifications is provided in Table 6.

In Figure 14 we have distinguished variable objects (blue for periodic; green for aperiodic) from the nonvariables (white) in the *Spitzer*/IRAC color–magnitude diagram. In the small Cha I sample, none of the periodic variables has an infrared excess suggestive of a disk. As was the case with σ Orionis (CH10), we can associate disks with the majority of aperiodic variables in our sample and lack of a disk with most of the periodic variables. But a number of objects do not fit these scenarios.

Five Cha I members display aperiodic variability but no sign of infrared excess in the *Spitzer* data. This curious small population of objects with rms values (∼0.01–0.03 mag) much lower than the other aperiodic variables and have Hα pEW and [3.6]–[8.0] values suggesting *absence* of accretion or an associated disk. In addition to light curves in which variability is clearly obvious by eye, these objects have χ^2 values high enough that their status as variables is not in doubt. All but one have $\chi^2 > 4.5$, or less than 10^{-5} probability that the light curve trends arose by chance; the remaining object (2MASS J05383922−0253084) has a χ^2 value of 2.85, or an estimated 0.4% probability that its light curve behavior is explained by noise. We show in Figure 15 the rms and infrared colors for Cha I members; Figure 15 of CH10 illustrates another such cluster of low-amplitude aperiodic variables with no signs of circumstellar disks.

A similar phenomenon was observed in the IC 348 cluster, in which a number of weak T Tauri stars (i.e., weak Hα) were found to be erratic variables by Littlefair et al. (2005). These results bring into question our ability to determine which cluster members are truly surrounded by disk material, which ultimately affects the analysis of rotation and possible disk locking. It appears from these light curves that a percentage of young objects retain enough gas and/or dust beyond the time that we would expect their disks to be fully cleared based on infrared observations. Alternatively, we may be viewing rapid evolution of magnetic spot features on the stellar surface.

REFERENCES

Bailer-Jones, C. A. L., & Mundt, R. 2001, A&A, 367, 218
Baraffe, I., Chabrier, G., Barman, T. S., Allard, F., & Hauschildt, P. H. 2003, A&A, 402, 701
Barrado y Navascués, D., Béjar, V. J. S., Mundt, R., et al. 2003, A&A, 404, 171
Barrado y Navascués, D., Zapatero Osorio, M. R., Béjar, V. J. S., et al. 2001, A&A, 377, L9
Beck, P. G., Montalban, J., Kallinger, T., et al. 2012, Natur, 481, 55
Béjar, V. J. S., Martín, E. L., Zapatero Osorio, M. R., et al. 2001, ApJ, 556, 830
Béjar, V. J. S., Zapatero Osorio, M. R., & Rebolo, R. 1999, ApJ, 521, 671
Béjar, V. J. S., Zapatero Osorio, M. R., & Rebolo, R. 2004, AN, 325, 705
Burningham, B., Naylor, T., Littlefair, S. P., & Jeffries, R. D. 2005, MNRAS, 356, 1583
Caballero, J. A. 2008, A&A, 478, 667
Caballero, J. A., Béjar, V. J. S., Rebolo, R., et al. 2007, A&A, 470, 903
Caballero, J. A., Béjar, V. J. S., Rebolo, R., & Zapatero Osorio, M. R. 2004, A&A, 424, 857
Cenko, S., Fox, D. B., Moon, D., et al. 2006, PASP, 118, 1396
Cieza, L., & Baliber, N. 2006, ApJ, 649, 862
Cieza, L., & Baliber, N. 2006, ApJ, 649, 862
Cieza, L., & Baliber, N. 2007, ApJ, 671, 605
Cody, A. M., & Hillenbrand, L. A. 2010, ApJS, 191, 389
Cody, A. M., & Hillenbrand, L. A. 2011, ApJ, 741, 9
Cohen, R. E., Herbst, W., & Williams, E. C. 2004, AJ, 127, 1602
Dawson, P., Scholz, A., & Ray, T. P. 2011, MNRAS, 418, 1231
Deeming, T. J. 1975, Ap&SS, 36, 137
Franciosini, E., Pallavicini, R., & Sanz-Forcada, J. 2006, A&A, 446, 501
Gastine, T., & Dintrans, B. 2011, A&A, 528, A6
Guenther, D. B., Kallinger, T., Zwintz, K., et al. 2009, ApJ, 704, 1710
Herbig, G. 1998, ApJ, 497, 736
Hernández, J., Hartmann, L., Megeath, T., et al. 2007, ApJ, 662, 1067
Joergens, V., Fernández, M., Carpenter, J. M., & Neuhäuser, R. 2003, ApJ, 594, 971
Kenyon, M. J., Jeffries, R. D., Naylor, T., Oliveira, J. M., & Maxted, P. F. L. 2005, MNRAS, 356, 89
Kurtz, D. W., Saio, H., Takata, M., et al. 2014, MNRAS, 444, 102
Lebreton, Y., & Goupil, M.-J. 2014, A&A, 569, 21
Lenz, P., & Breger, M. 2005, CoAst, 146, 53
Littlefair, S. P., Naylor, T., Burningham, B., & Jeffries, R. D. 2005, MNRAS, 358, 341
Lodieu, N., Dobbie, P. D., & Hambly, N. C. 2011, A&A, 527, 24
Lodieu, N., Zapatero Osorio, M. R., Rebolo, R., Martín, E. L., & Hambly, N. C. 2009, A&A, 505, 1115
Luhman, K. L. 2004, ApJ, 602, 816
Luhman, K. L. 2007, ApJS, 173, 104
Luhman, K. L., Allen, L. E., Allen, P. R., et al. 2008, ApJ, 675, 1375
Luhman, K. L., Hernández, J., Downes, J. J., Hartmann, L., & Briceño, C. 2008, ApJ, 688, 362
Luhman, K. L., Lada, E. A., Muench, A. A., & Elston, R. J. 2005, ApJ, 618, 810
Luhman, K. L., & Muench, A. A. 2008, ApJ, 684, 654
Luhman, K. L., Stauffer, J. R., Muench, A. A., et al. 2003, ApJ, 593, 1093
Martí, B. L., Eislöffel, J., Scholz, A., & Mundt, R. 2004, A&A, 416, 555
Martín, E. L., Delfosse, X., & Guieu, S. 2004, AJ, 127, 449
Muench, A. A., Lada, C. J., Luhman, K. L., Muzerolle, J., & Young, E. 2007, AJ, 134, 411
Mužić, K., Scholz, A., Geers, V., Fissel, L., & Jayawardhana, R. 2011, ApJ, 732, 86
Palla, F., & Baraffe, I. 2005, A&A, 432, L57
Pecaut, M. J., Mamajek, E. E., & Bubar, E. J. 2012, ApJ, 746, 154
Preibisch, T., Brown, A. G. A., Bridges, T., Guenther, E., & Zinnecker, H. 2002, AJ, 124, 404
Scholz, A., & Eislöffel, J. 2004, A&A, 419, 249
Scholz, R.-D., Brunzendorf, J., Ivanov, G., et al. 1999, A&AS, 137, 305
Sherry, W. H., Walter, F. M., & Wolk, S. J. 2004, AJ, 128, 2316
Sherry, W. H., Walter, F. M., Wolk, S. J., & Adams, N. R. 2008, AJ, 135, 1616
Slesnick, C. L. 2008, PhD thesis, California Institute of Technology
Slesnick, C. L., Hillenbrand, L. A., & Carpenter, J. M. 2008, ApJ, 688, 377
Zapatero Osorio, M. R., Caballero, J. A., Béjar, V. J. S., & Rebolo, R. 2003, A&A, 408, 663
Zwintz, K. 2008, ApJ, 673, 1088
Zwintz, K., Fossati, L., Ryabchikova, T., et al. 2014, Sci, 345, 550